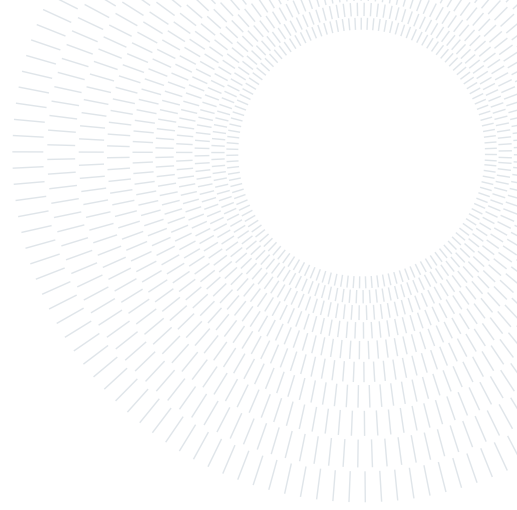




POLITECNICO
MILANO 1863

SCUOLA DI INGEGNERIA INDUSTRIALE
E DELL'INFORMAZIONE



DNS investigation of turbulent flow over a circular recess

TESI DI LAUREA MAGISTRALE IN

AERONAUTICAL ENGINEERING - INGEGNERIA AERONAUTICA

Julien Cerutti, 968803

Advisor:

Prof. Maurizio Quadrio

Co-advisors:

Alessandro Chiarini
Federica Gattere

Academic year:

2022-2023

Abstract: The turbulent flow over an isolated recess is characterized, as a consequence of the increasing interest in the so-called dimples, to shed light on its ability to impose a spanwise motion on the flow and reduce drag. The work is based on DNS simulations of a circular recess with a depth-to-diameter ratio of 0.05 placed inside a channel. Turbulent simulations at $Re_\tau = 180$ have been carried out and compared to the laminar counterpart. The flow over the recess presents a converging-diverging pattern and creates a spanwise motion, mainly driven by the pressure gradient, similar to the one observed with the spanwise forcing drag reduction methods. The presence of the recess provides a variation of the skin friction, with very similar values for the laminar and turbulent solutions in the upstream half, but with different behavior in the downstream one: the difference in the results seems to be tied to an increase in the Reynolds shear stress, that was pictured using a variation of the FIK decomposition [6] which allowed to split the skin friction into a laminar and turbulent part. Some hints on how to modify the geometry of the recess to possibly achieve drag reduction are provided.

Key-words: dimples, flow control, drag reduction, turbulence

1. Introduction

The interest in the flow configuration considered in the present work descends from the so-called dimples and their debated ability to reduce aerodynamic drag. Dimples are small recesses imprinted on a surface, well known for their use on bluff bodies, being able to affect the turbulent boundary layer and flow separation [5] (for example their application on golf balls), as well as their capability to enhance the convective heat transfer of a surface with a relatively small penalty on the pressure drop [3]. It is only in recent years, starting from the works of Alekseev et al. 1998 [1] and Lienhart et al. 2008 [12] that there is an increasing interest in the investigation of the drag proprieties of dimples imprinted on a flat surface and their application to produce drag reduction. The drag control has always been a topic of great discussion and interest for the economic implications it entails: a reduction in drag of even 1% would represent a substantial gain for many engineering fields, from aviation to automotive [25]. For a flat wall the total drag is represented by the skin friction, which represents the most essential manifestation of the dissipative nature of turbulence. For this reason, several methods are available to reduce the friction drag below the level typically required for a smooth wall. They can be categorized into two main groups: active, which requires extra energy, and passive, where the results depend only on the geometry of the wall. The former produces larger savings, but the requirement for added energy causes an increase in complexity and costs, making the passive methods a more practical solution. One

of the most famous examples of the latter is represented by riblets [7] which consist of streamwise-aligned microgrooves. Although their efficiency in reducing drag has been largely discussed, they present non-negligible maintainability issues [24], as mechanical problems caused by the increase in weight due to their application, thus making them difficult to utilize in practice. Concerning the active drag reduction, one of the most studied categories is represented by the spanwise forcing methods (like the oscillating walls technique [10, 18] and the traveling waves [19]). They are based on the idea of generating a spanwise oscillation in the flow, enhancing the near-wall stability to reduce the viscous drag. In this work we aim at investigating, starting from the study of an isolated recess, whether dimples may induce a similar spanwise motion of the near wall-flow as suggested by some authors [30, 33], thereby overcoming the downside (external energy needed) of the active drag reduction methods and passively reduce drag.

The effect of the dimples on the flow strongly depends on their geometry, in particular on the depth (d) to diameter (D) ratio [11]. Dimples used for the enhancement of heat transfer normally have a depth-to-diameter ratio of 0.2-0.5, to generate vortical structures that greatly influence the Nusselt number [3, 26]. For drag reduction, instead, shallow dimples with a d/D ratio of 0.1 or less are studied. Beyond the hypothesis behind the working mechanism of the dimples over the past few years several studies, both numerical and experimental, were performed over surfaces using recesses with different shapes and geometries, to find a configuration that could lead to a drag reduction, providing however contradictory results. Some studies have reported a drag reduction [28, 33, 34]) while others have found a drag increase [12, 20, 31]). Two main mechanisms are proposed to reduce drag: for higher d/D (around 0.1) a phenomenon called tornado-like vortex is presented, while for lower ratios the flow exhibits a convergent-divergent pattern, generating a velocity in the spanwise direction and leading to the idea presented before that the dimples can be used to create a passive spanwise forcing. The difficulty in obtaining coherent results is clearly highlighted by the two experiments of Van Nesselrooij. In 2016 [33] they found a drag reduction while in 2022, with the same geometry but a better experimental apparatus [32], a drag increase was observed [29]. According to Gattere et al. 2022 [8] one of the causes behind this discrepancy in the results is the lack of replicability for the various experiments and the correct definition of the equivalent volume over a dimpled wall. When comparing, in a channel flow, the drag properties between the flat wall and the one covered in dimples, the reference height of the latter must be adjusted, leading to the choice of the correct Reynolds number, to perform the correct comparison between the two cases. This correction has to be applied also to the bulk velocity and, if the simulations are carried out using a DNS (Direct Numerical Simulation), to the volume force applied to the flow [8].

Consequently, looking at the literature related to dimples both the results on the drag performances and the hypothesis behind their applications appear to be very confused, causing the lack of a solid foundation from which to begin a study of a geometry that can, indeed, lead to a drag reduction. Therefore the purpose of this work, which is based on a Direct Numerical Simulation (DNS), is to study in depth the influence of a circular recess (Fig.1) on the turbulent flow, accurately characterizing the statistics within it, especially the spanwise motion. This will allow us to gain some hints on the manipulation of the recess geometry to modify the flow behavior and possibly achieve drag reduction when positioned into an array. The turbulent simulations will be compared to the laminar counterpart, to understand whether the laminar flow alone provides significant explanations of the phenomena and how these are affected by the turbulent properties.

This study follows, inevitably, all that strand of works on cavities widely debated in the past years, over which the behaviour of the flow has been largely discussed. It is also true, however, that most of the efforts are concentrated on rectangular and two-dimensional cavities or otherwise geometries in which there is a significant separation. An example of recent studies on 3D circular cavities are the works of Scarano [22, 23], where their influence on the turbulent boundary layer and the possibility of achieving drag reduction by using it in a suitably positioned array are studied. The recesses used in dimpled surfaces for drag reduction have at their base the idea of a more delicate geometry, with a continuous depth variation from the flat wall to their deepest point, which limits the separation within them, going only to change the direction of the mean flow: represents the limiting case, in this sense, the tornado-like mechanism introduced before, which consist in the creation of a vortex inside the recess, that however seems to the authors less likely applicable, while the utilization of dimples to generate a spanwise motion appears to be a more promising way, also because, as observed in [8], shallower dimples usually provide better results in terms of drag reduction.

The present contribution is structured as follows. In section §2 the methodology and the numerical code used to perform the simulations are discussed, while in section §3 the results are presented, with a focus on the spanwise motion and the comparison between the properties of the turbulent flow and the laminar solutions. Lastly, section §4 contains a discussion of the results, with some ideas on how to modify the geometry to change the flow behavior.

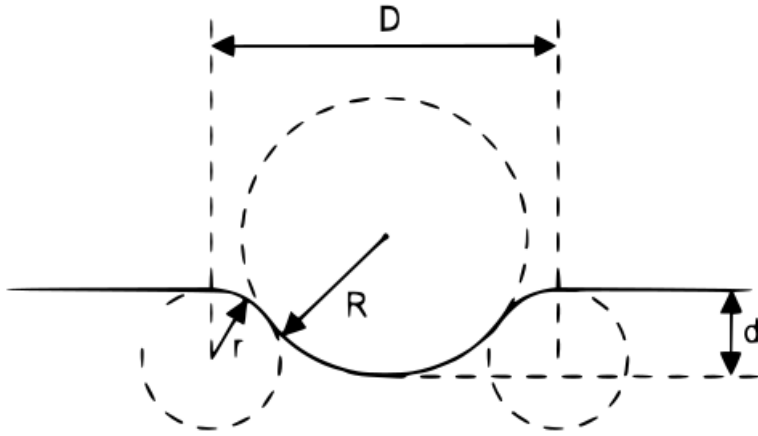


Figure 1: Lateral section of the recess. Image from [32].

2. Methodology

2.1. Recess geometry

The simulations are carried out on an isolated recess, placed in the bottom wall of an indefinite channel with a reference half-height between the two flat walls of $\delta = 1$. A circular recess is studied, being one of the most popular and, at the same time, simple geometry used in dimples arrays; in particular, the same circular shape used by [15] is adopted, which is also similar to the geometry used by [27, 28]. The lateral section of the recess is made up of three circles, as shown in Fig.1, two of radius r (edge radius), which form the small rounded edge, and one R (bottom radius): the geometry can be visualized, in 3 dimensions, as the union of a spherical indentation of radius R and a torus with inner dimension r . The purpose of the round edge, as reported by Mitsudharmadi et al. 2009 [14], is to mitigate abrupt flow modifications when the fluid flows over the recess, reducing the occurrence of separations. The other two main parameters used to describe the geometry are the diameter D and the depth d . Relations between them exist [4] and can be expressed as

$$R = \frac{d}{2} + \frac{D_n^2}{8d} \quad (1)$$

$$\frac{D}{2} = \sqrt{d(2R + 2r - d)} \quad (2)$$

where D_n is the nominal diameter, being specifically the diameter of the circle obtained in the intersection between the sphere (R) and the horizontal plane. The depth-to-diameter ratio of the present recess is $d/D = 0.05$, which is one of the most diffused, with $D = 5\delta$ and $d = 0.25\delta$, the same used by [15]. Following the relations of Eq.1 and 2 the dimensions are reported in table 1.

R	r	D	d
8.415δ	4.21δ	5δ	0.25δ

Table 1: Recess dimensions, from [15].

2.2. Governing equations and numerical method

The computational domain consists of a channel divided into two streamwise-adjacent portions (Fig.2): the upstream volume with planar walls, that runs a standard flat channel simulation, is streamwise-periodic and feeds the downstream one where inflow and outflow conditions are used. Namely, for the outflow velocity Neumann conditions are applied, periodic ones are used everywhere for the spanwise direction and non-slip and no penetration boundary conditions are used at the wall. Fig.2 shows the global reference axes, whose direction (x,y,z) correspond, respectively, to the streamwise, spanwise, and wall-normal ones. The flow is governed by the incompressible Navier Stokes equations (3) for velocity $\mathbf{u} = [u \ v \ w]$ (streamwise, spanwise, and wall-normal component) and pressure p :

$$\begin{cases} \nabla \cdot \mathbf{u} = 0 \\ \frac{\partial \mathbf{u}}{\partial t} + (\mathbf{u} \cdot \nabla) \mathbf{u} + \nabla p = \frac{1}{Re_\tau} \nabla^2 \mathbf{u}, \end{cases} \quad (3)$$

The Reynolds number is defined as $Re_\tau = u_\tau \nu / \delta$, where δ is the channel half-height, ν the fluid viscosity and $u_\tau = \sqrt{\tau_w / \rho}$ is the friction velocity, expressed in terms of wall friction and density (which is considered unitary), computed on the flat wall. The simulations are performed using a *CPG* (Constant Pressure Gradient) approach [17]), which consists in the utilization of a constant forcing term in the periodic channel.

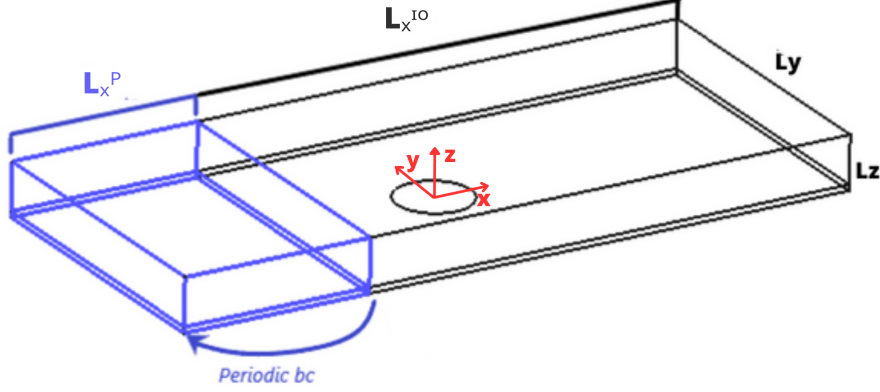


Figure 2: Sketch of the computational domain. The streamwise-periodic upstream domain (blue) provides an inflow condition for the downstream one (black). The recess is located on the lower wall in the inlet-outlet part.

The equations are integrated in time using a DNS code, introduced by Luchini [13] and already used in different works, based on second-order finite differences on a staggered grid. The time advancement is performed employing a fractional step with a fully explicit third-order Runge Kutta method. The presence of the domain is dealt with using an immersed boundary method (IBM).

The code works in parallel and its parallelization is strictly connected to the domain characteristics (Fig.2). The total number of points in x is equally divided by the number of processors (N_{proc_x}) assigned in this direction, then some of these ($N_{proc_{xp}}$) are given to the periodic part and all the others ($N_{proc_x} - N_{proc_{xp}}$) to the inlet-outlet one. To optimize the number of processing elements used in the simulations (thus improving the time-cost balance), a strong scaling performance was implemented on the code, i.e. with the dimension of the problem settled up the number of processors was increased, computing for each case the amount of time needed to perform a task. In particular the *Speedup*, defined as $Speedup = t(1)/t(N_p)$ was studied, where $t(1)$ is the amount of time needed to perform a serial task, and $t(N_p)$ is the amount of time to complete the same unit of work with N_p processing elements. It's important to observe that, due to the nature of our code, the minimum number of processors that can be used is 2, one for the period half of the domain and the other for the inlet-outlet part, making it impossible to perform a serial computation and forcing to compute the speedup using this configuration as the slowest reference case, namely

$$Speedup = \frac{t(2)}{t(N_p)} \quad (4)$$

As Fig.3 shows the required time to compute 10 iterations is almost halved up to 16 processors, meaning an increase in performances of 100%, which decreases to 80% for 64. The number of processors adopted was 48, in order to balance the efficiency with the actual time needed to complete the simulations, which is also the maximum number of processing elements available in 1 node of the cluster used to complete the computations.

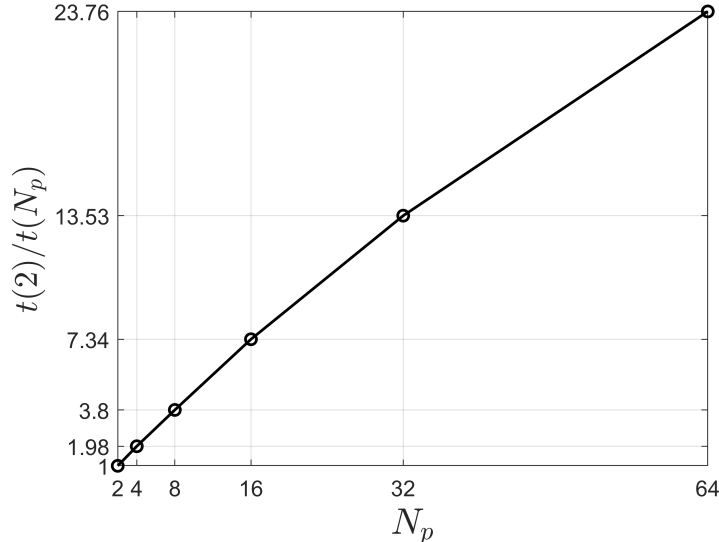


Figure 3: Time performance analysis for the numerical code. The Speedup is computed using the time required to perform 10 iterations with the grid adopted.

2.3. Grid and computational domain

The Reynolds number used to carry out the simulations is $Re_\tau = 180$, based on the flat channel. The size of the domain (Fig 2) is $(L_x^P + L_x^{io}, L_y, L_z) = (28.68, 12.5, 2.25)$ in the stream-wise, span-wise and wall-normal directions respectively and is discretized with $(N_x^P + N_x^{io}, N_y, N_z) = (864, 606, 308)$ points, where the superscript "P" indicates the periodic channel while "io" the inlet-outlet part. The flat walls are placed at $z = 0.25$ and $z = 2.25$ and the recess, located in the downstream-non periodic part, is carved inside the wall and reaches $z = 0$ in its lowest point, which corresponds to the center of the indentation where the origin of the axis is located (Fig.2). The upstream-periodic part extends between $x = -14.5$ and $x = -6.5$ ($L_x^P = 8$) and has a streamwise spatial resolution of $N_x^P = 180$ discretization points, while in the wall-normal direction, out of $N_z = 308$, only 158 points are actually in the flow, since the Cartesian grid extends between $z = 0$ and $z = 2.25$ but below $z = 0.25$ all the points are inside the solid wall. The downstream portion of the computational domain starts at $x = -6.5$ with a length of $L_x^{io} = 20.86$ and $N_x^{io} = 684$ points non-evenly distributed. Here the center of the recess is placed at a distance $x = 6.5$ from the inlet, to avoid its influence and allow the flow to completely expand after the end of the indentation. In the spanwise direction it is located at the center of the channel, at $y = 0$ (at $y = 6.25$ from the side of the domain), resulting in a distance of $y = 7.5$ between the lateral side of two recesses (accounting the y-periodicity) equivalent to three radii. This is done to avoid problems caused by the lateral periodicity of the channel, keeping the recess isolated and eliminating the risk of mutual interaction. The streamwise resolution is constant $\Delta x^+ = 8$ in the upstream part but increases as the recess is approached, reaching up to $\Delta x^+ = 3.5$, to improve the refinement over it. The subscript + indicates that the dimensions are written in the viscous scales, i.e. divided by $\delta_\nu = \nu/u_\tau$, based on u_τ on the flat channel. In the spanwise direction the $N_y = 606$ points are non-evenly distributed, with the refinement that varies from $\Delta y^+ = 5$ on the flat wall to $\Delta y^+ = 3$ on the recess. The wall-normal spacing is neither constant in z nor symmetrical with respect to the centreline, since the recess is present on the lower wall. A constant $\Delta z^+ = 0.3$ is adopted from the bottom of the recess to the flat wall, then Δz^+ gradually increases until, at the centerline, the maximum value of $\Delta z^+ = 4$ is reached. The spacing then decreases again in the upper half of the channel, to reach $\Delta z^+ = 0.8$ at the upper wall. The resolution in spanwise and wall-normal direction is the same used for both the periodic and inlet-outlet domains, to avoid interpolation. The grid size on the recess is similar to the one suggested in [29] and adopted in [15], in order to catch all the phenomena within it. Overall, on the flat surface, the largest streamwise spacing is around eight times the local Kolmogorov length η , while is everywhere under 5η for the spanwise direction and under η for the wall normal one. Near the recess the resolution is even higher, with the spanwise grid size under 3η and the streamwise one below 3.5η , while the wall-normal is again lower than η . The simulations were performed using a CFL (Courant–Friedrichs–Lewy) number of 1.5, for a time in viscous unit of over 10000.

The results presented will be scaled on u_τ and δ_ν , unless otherwise indicated. The dimensions expressed in viscous units will be marked by the "+" symbol, following the notation used until now. The ones without it are expressed in external units, specifically made dimensionless by the reference channel half-height δ . The spatial dimensions in x and y will be presented scaled by the dimple diameter D .

Throughout the thesis, we will employ the Reynolds decomposition, i.e. $\mathbf{u} = \bar{\mathbf{U}} + \mathbf{u}'$, where $\bar{\mathbf{U}}$ is the time-averaged velocity field and \mathbf{u}' is the fluctuating velocity field. The same convention holds for the pressure field. We will use the over-bar to indicate a time-averaged value, in particular we will indicate the mean values with capital letters superscript with the bar.

2.4. Laminar simulations

To understand the behavior of the flow inside the recess and the influence of turbulent properties a laminar simulation at the same Re_b of the turbulent case (≈ 2800) was performed, with $Re_b = U_b \delta / \nu$, where $U_b = 1/\delta \int \bar{U}(z) dz$ is the bulk velocity, δ is the channel half height and ν is the viscosity. Being the Reynolds number sufficiently low, it was possible to use this same value for both simulations, keeping the flow laminar if not perturbed. The grid used for the laminar case was composed of $(N_x^P + N_x^{io}, N_y, N_z) = (492, 300, 191)$ points, and a shorter domain with dimensions $(L_x^P + L_x^{io}, L_y, L_z) = (20.2, 12.5, 2.25)$, where $L_x^P = 4$, was used. The simulations required quite high resolutions, although laminar, in order to have the immerse boundary provide a good refinement of the geometry and to avoid errors while computing the recirculation zone after the recess leading edge, observed in the turbulent flow and consequently expected also in the laminar case. Computing the laminar simulations was, however, faster than the turbulent ones, performing the same tasks with the same number of processors in one-third of the time. The simulations used the same CPG approach adopted in the turbulent case, thus also these results will be presented scaled by the relative friction velocity in order to have the skin friction reference value of 1 over the flat wall.

3. Results

3.1. Turbulent and laminar mean flow

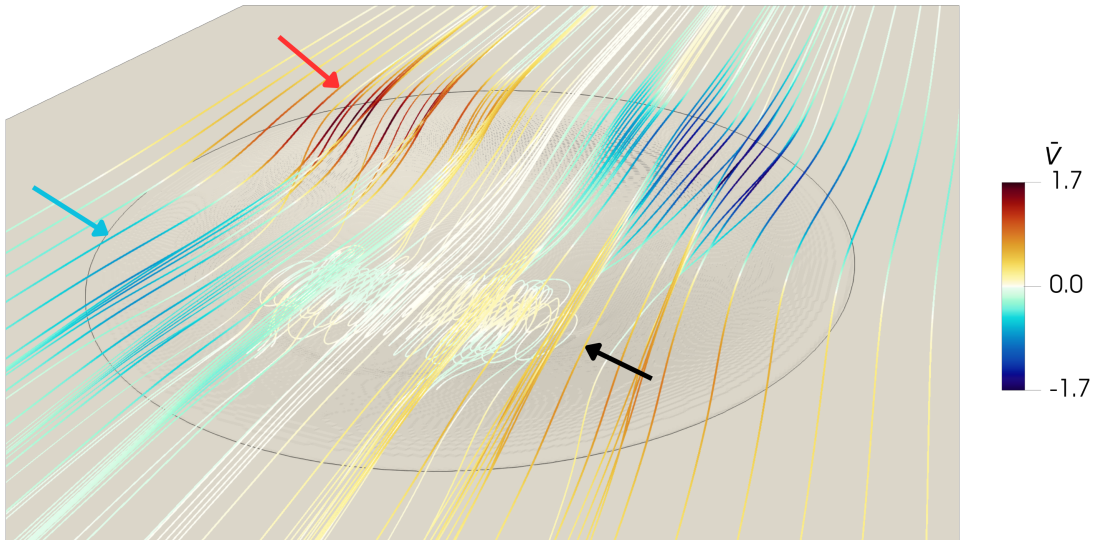


Figure 4: Streamlines over the recess for the mean flow field of the turbulent case. The flow direction is from the bottom left to the upper right corner. The streamlines are colored using the spanwise velocity and the recess contour is highlighted by the black circle. The black arrow indicates the separation while the blue and red ones point, respectively, the convergent and divergent motion.

In this section the mean flow for the turbulent and laminar cases will be characterized, comparing the two different solutions for the present geometry.

Fig.4 shows the streamlines over the recess, colored using the mean spanwise velocity of the turbulent simulations. They are plotted from a series of seeding vertical lines placed inside the recess, evenly spaced in spanwise direction, and one horizontal extended between $y/D = -0.75$ and $y/D = 0.75$ at $z^+ = 9$ (from the flat wall). The mean profile shows a convergent-divergent behavior, indicated, respectively, by the blue and the red arrows. The recirculating zone, visible in the first half of the recess and pointed by the black arrow, corresponds to the one found in [15] and predicted in [11]: decreasing d/D the separation weakened and eventually disappears, while increasing it the reattachment point would move downstream till the end of the recess and the flow pattern

change, from diffuser-confuser to tornado-like vortexes (as introduced in §1).

Fig.5a shows the profiles of turbulent mean streamwise flow as a function of the vertical coordinate near the wall, between $z^+ = 0$ and $z^+ = 100$ in the symmetry plane $x - z$ at $y/D = 0$. Moving down to the first half of the recess the slope of $\bar{U}(z)$ decreases, following the curvature of the wall. At $x/D = -0.2$ the negative value of \bar{U} indicates the separation, which is highlighted in Fig.7a, that reaches its maximum dimension in the centerline and extends between $-0.3 < x/D < -0.05$. According to [15] the separation increases the total drag of the dimple, ruining the streamwise alignment of the mean flow provided, instead, by one with a gentler wall slope in the upstream half. On the downstream side the slope of $\bar{U}(z^+)$ increases, becoming very steep at $x/D = 0.4$ where the concavity of the wall changes, at the transition between the bottom radius (R) to the rounded edge (r). Moving in the spanwise direction along the $y - z$ plane at $x/D = 0$ (Fig.5b) from the edge of the recess to the center, the slope of $\bar{U}(z^+)$ decreases gradually, from the reference flat value to the one computed at the center, showing that the influence of the indentation increases quite regularly along the lateral span. This highlights also that the effect of the recess in the spanwise direction on the streamwise component is perceived only inside its radius, since the streamwise mean flow lapping the lateral edge ignores its presence. In the streamwise direction, instead, its influence on \bar{U} is perceived up to $x/D = 0.8$ (Fig.5a) where the velocity profiles eventually collapse into the reference flat ones.

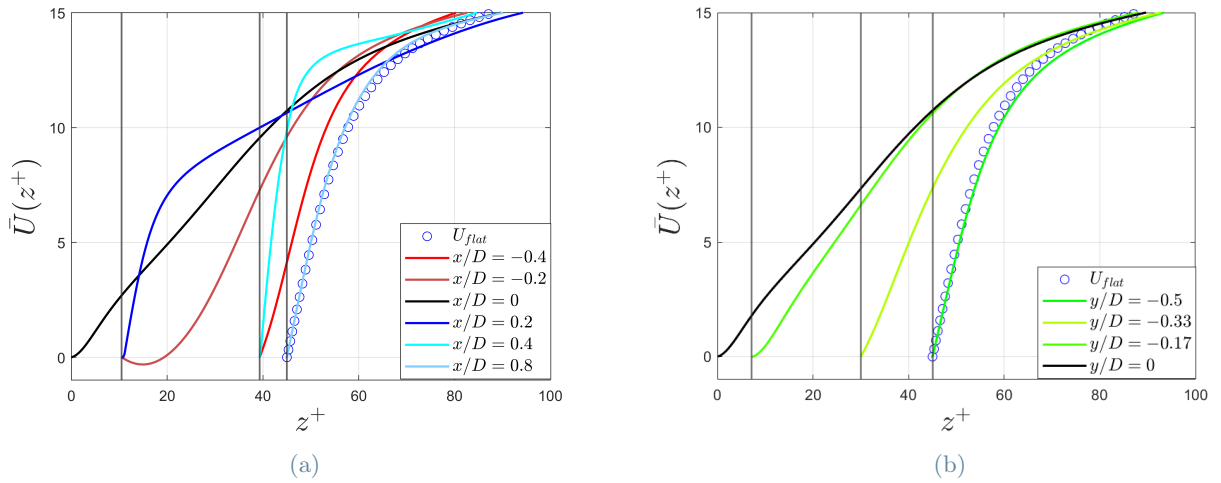


Figure 5: $\bar{U}(z)$ vertical profiles plotted at different streamwise and spanwise positions. (a) Plane $x - z$ at $y/D = 0$. (b) Plane $y - z$ at $x/D = 0$. The vertical black lines indicate the local wall height.

In Figure 6 \bar{U} is plotted at $z = 0.0055$ ($z^+ = 1$ for the turbulent case) from the flat wall for the turbulent (6a) and laminar (6b) solutions, allowing a direct comparison between the two cases. In the turbulent one the streamwise velocity grows while moving downstream along the recess, reaching the maximum value near the trailing edge, following the increment of $d\bar{U}/dz^+$ observed in Fig.5. The trend is similar for the laminar solutions, although the values involved are lower. Fig.7 pictures, in the $x - z$ plane at $y/D = 0$, the separation that occurs at the leading edge of the recess that, for the two cases, is limited within it. In the turbulent (Fig.7a), as was already observed in Fig.5a and 4, the separation is located only in the upstream half, with the reattachment point located slightly before $x/D = 0$, while in the laminar case (Fig.7b) it covers almost all the indentation, extending between $x/D \approx -0.35$ and 0.3 .

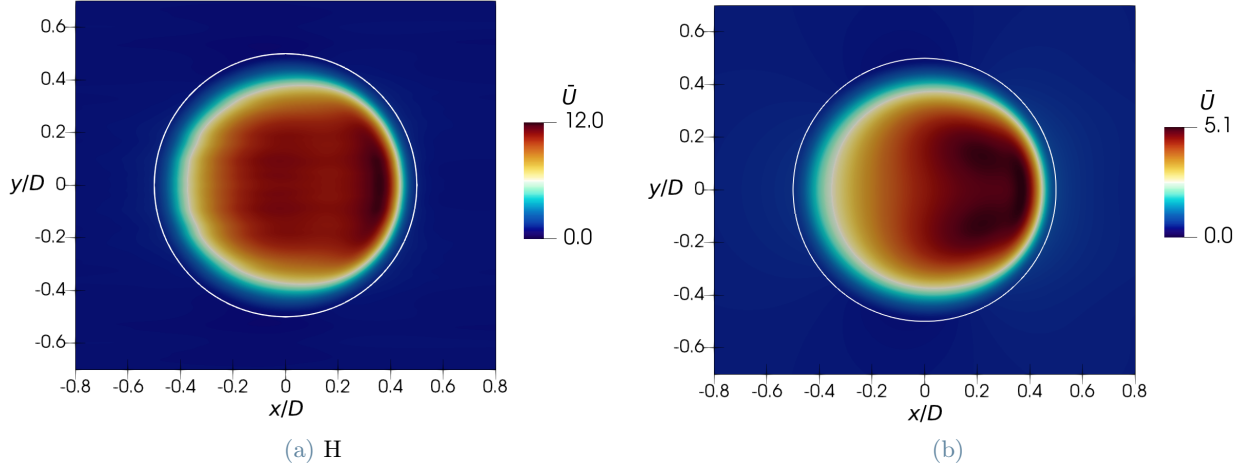


Figure 6: \bar{U} in the $x - y$ plane at $z = 0.0055$ from the flat wall for the turbulent (a) and laminar case (b). The recess contour is indicated by the white circle.

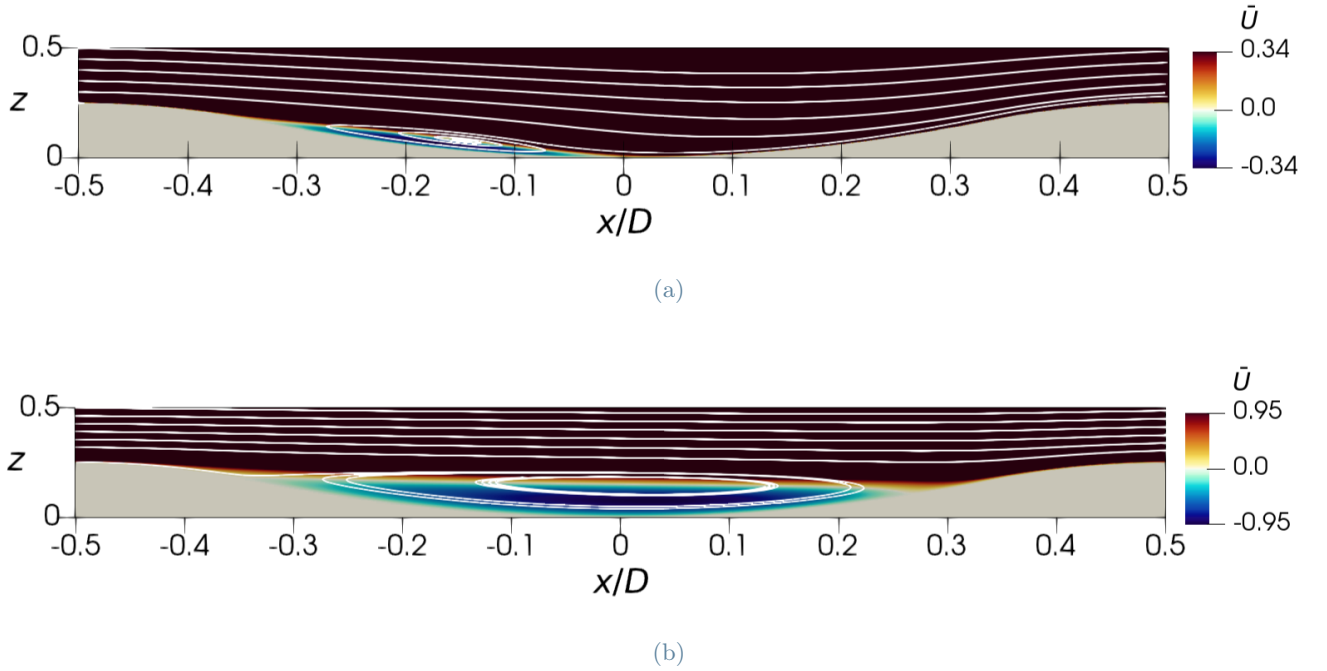


Figure 7: Highlights of the separation for the turbulent (a) and laminar case (b).

Figure 8a reports for the turbulent case the mean wall-normal flow as a function of the vertical coordinate in the $x - z$ plane at $y/D = 0$ for $1 < z^+ < 200$. Starting from the leading edge the negative $\bar{W}(z^+)$ growth while moving to the center, where it changes in sign becoming positive in the downstream half, where higher values than the ones in the upstream part are reached. The maximum value of \bar{W} at $x/D = 0.4$ is, for example, almost twice the one at $x/D = -0.4$. This is visible also in Fig.9a, which shows the plot of \bar{W} in the $x - y$ plane at $z = 0.4$, where it can be observed, moreover, that in the streamwise direction the behavior is not symmetrical. This is caused by the convection of the flow and will be seen in most of the phenomena over the recess. It is even clearer in the laminar simulations (Fig.9b) where the asymmetry in x is greater and \bar{W} is mainly negative over the recess. The values are lower than in turbulent case, but again the ones on the downstream side are higher than the correspondent in the upstream half. Looking in the spanwise direction, Fig.8b shows that the intensity of \bar{W} increases quite regularly from the edge (where is almost zero) to the center: this, together with Fig.9a, highlights that the influence of the recess on the wall-normal velocity is limited, in the spanwise direction, inside its radius, while it extends up to $x/D = 0.8$ in the streamwise one. In the laminar case, the recess appears to have a greater influence on the outside flow, creating a distinct area of negative and positive \bar{W} before and after its centerline and being perceived, in the streamwise direction, till $x/D = 1$. Nevertheless, as Fig.8a shows the

recess generates a vertical motion in the flow, which is perceived up to the opposite flat wall over it.

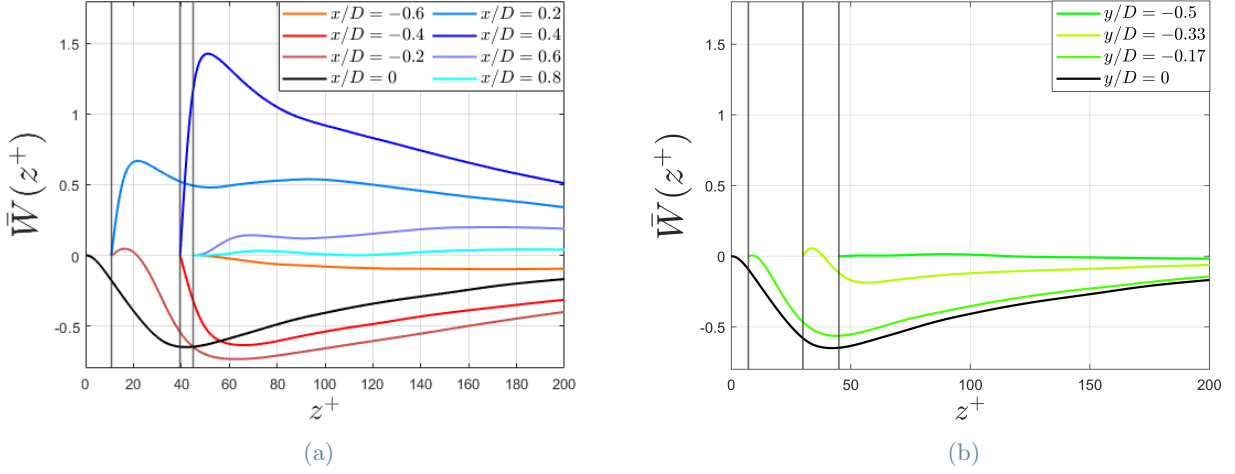


Figure 8: $\bar{W}(z)$ vertical profiles plotted at different streamwise and spanwise positions. (a) Plane $x - z$ at $y/D = 0$. (b) Plane $y - z$ at $x/D = 0$. The vertical black lines indicate the local wall height.

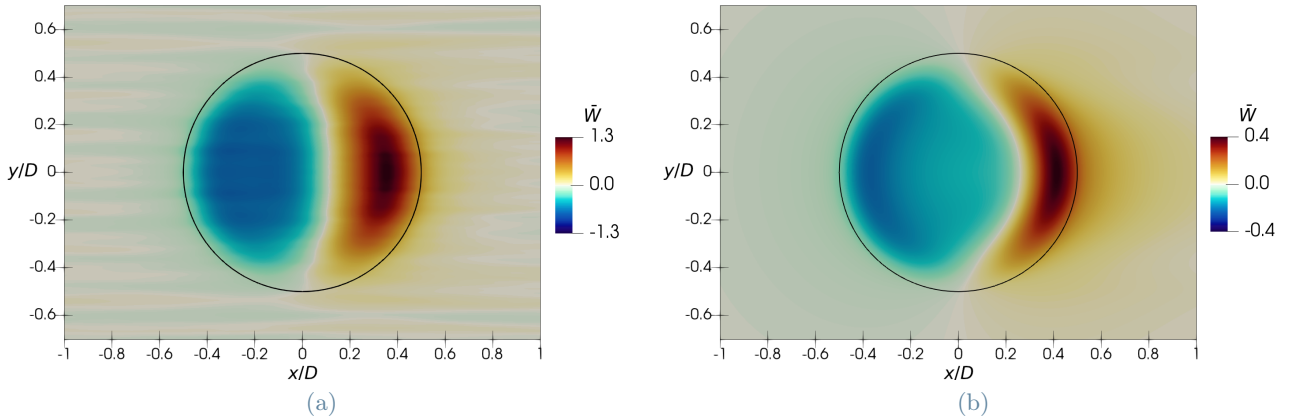


Figure 9: $\bar{W}(z)$ plot in the $x - y$ plane at $z = 0.4$ for the turbulent (a) and laminar solutions (b). The recess contour is indicated by the black circle.

Fig.10 shows the plot of the spanwise velocity field over the recess, taken in the plane $x - y$ at $z = 0.4$, for the turbulent (10a) and laminar (10b) solutions. The converging-diverging pattern observed in Fig.4 is visible for both cases and leads to the immediate observation of the anti-symmetric behavior of \bar{V} across the $x - z$ plane passing through the recess centerline. Also the spanwise velocity presents an asymmetry in the streamwise direction, and the values generated in the downstream half of the recess are more intense than the ones in the upstream side, making the diverging motion stronger than the converging one, as observed also by [29] and in the particle image velocimetry (PIV) of Van Campenhout et al. 2016 [30]. The asymmetry is, again, more pronounced in the laminar case (Fig.10b), although the converging and diverging values are closer than the ones of the turbulent simulations (the negative and positive peaks at the dimple leading and trailing edge are very similar). Fig.11a and 11b show, respectively, the distribution of $\bar{V}(z^+)$ in the $x - z$ plane at $y/D = -0.25$ and in the $y - z$ plane at $x/D = 0$ for the turbulent (solid line) and laminar case (dashed line). The three positions in Fig.11a where $\bar{V}(z^+)$ is plotted were chosen because indicative of the different behavior of the two solutions. It is here observable, especially at $x/D = -0.2$ and $x/D = 0$, that $\bar{V}(z^+)$ in the turbulent case presents a very steep variation moving from the negative to the positive values (for example at $x/D = 0$ between $z^+ = 22$ and 40) absent in the laminar simulation. This is observable also in spanwise direction (Fig.11b) where along y at $x/D = 0$ the slope of $\bar{V}(z^+)$ between positive and negative values increases moving to $y/D = -0.33$. From Fig.10a is possible to observe that, unlike what happened for \bar{U} and \bar{W} , in the turbulent case the recess influences the spanwise velocity outside its area in both x and y directions: in the first, its effect is perceived already at $x/D = -0.8$ and up to $x/D = 1.4$, while in the second, \bar{V} is non zero till $y/D = -0.75$ (Fig.10a).

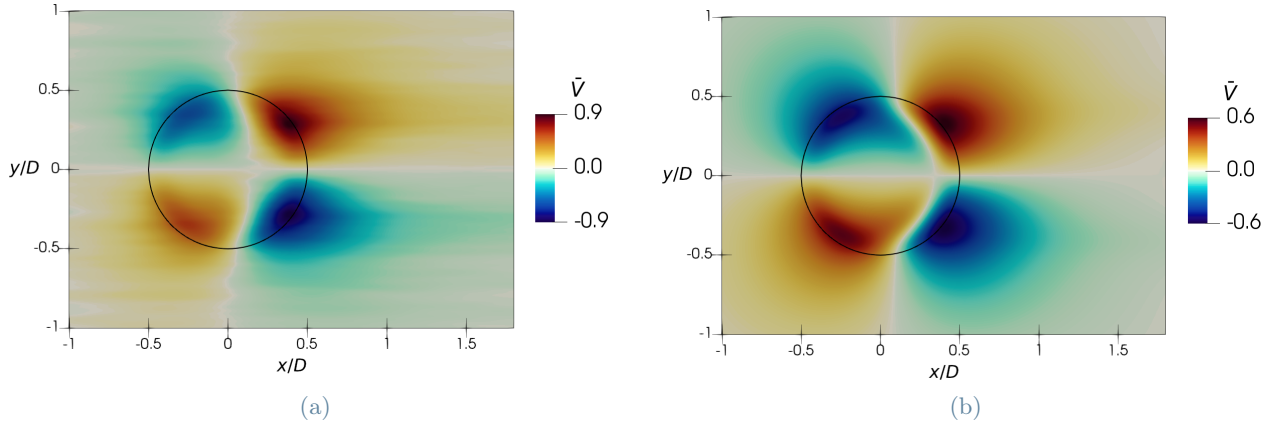


Figure 10: $\bar{V}(z)$ plot in the $x - y$ plane at $z = 0.4$ for the turbulent (a) and laminar solutions (b). The recess contour is indicated by the black circle.

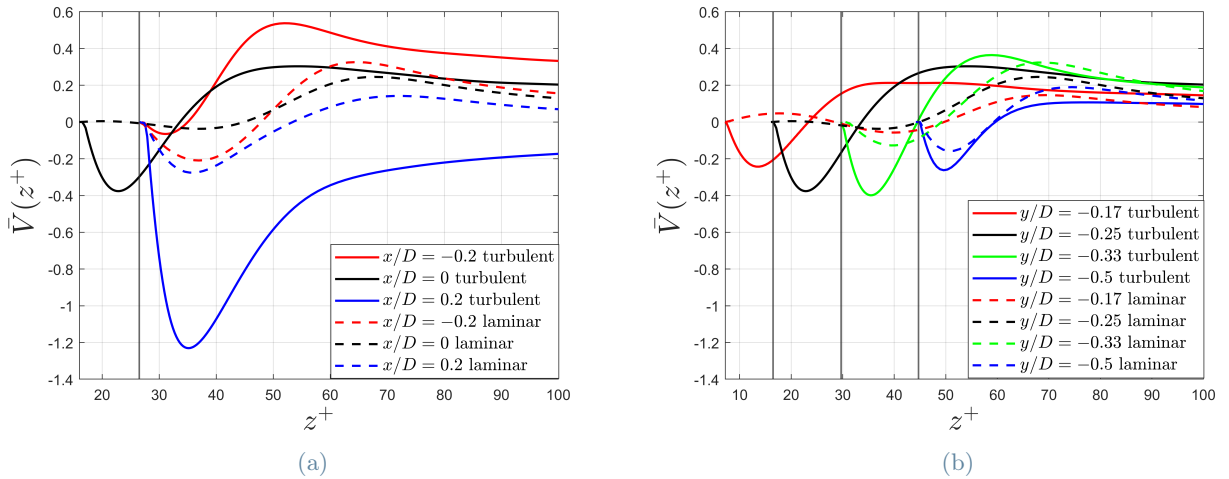


Figure 11: Values of $\bar{V}(z)$ for laminar (dashed lines) and turbulent (solid lines) simulations, taken in the plane $x - z$ at $y/D = -0.25$ (a) and in the plane $y - z$ at $x/D = 0$ (b). The vertical black lines indicate the local wall height.

The behavior is similar for the laminar case (Fig.10b).

The fact that the influence of the recess in the velocity field \bar{V} extends outside its area indicates how important, especially when speaking of these recesses as a way of generating a spanwise forcing, the mutual interaction between them is, since the velocity \bar{V} generated in one will inevitably go on to affect the others and vice versa. The variation in the sign of \bar{V} along z (Fig. 11a) suggested the presence of turbulent vortical structures aligned with the streamwise direction inside the recess. This was investigated using the λ_2 method [9] on the turbulent case. In Fig.12 (flow from bottom left to top right), the isosurfaces of $\lambda_2^+ = -0.04$ for an instantaneous flow field are plotted. The arrow indicates the structure observable in the center, which generates around $x/D = 0$ from the line of vortices coming from upstream and extends in the downstream side, evolving in sort of oval shape around the central axis up to the trailing edge, justifying the steeper variation of $\bar{V}(z^+)$ in the turbulent case observed in Fig.11. The presence of these structures seems to be tied to the geometry of the wall, since they are located in the downstream half of the recess, following its shape and being spread, in the vertical direction, between $z^+ = 0$ and $z^+ = 100$. They were observed for several instantaneous flow fields.

In Fig.13 the distributions of pressure in the two cases are compared. For both its value is set equal to zero at the outlet and the behavior observed is very similar: the pressure decreases at the leading edge, increases moving inside the recess and then decreases again at the trailing edge. In the turbulent (Fig.13a) case higher values are reached, especially in the downstream half, while in the laminar one (Fig.13b) the decrease at the trailing edge is less extended. Nevertheless, in both cases \bar{P} is greater near the center of the recess i.e. where the wall is steeper.

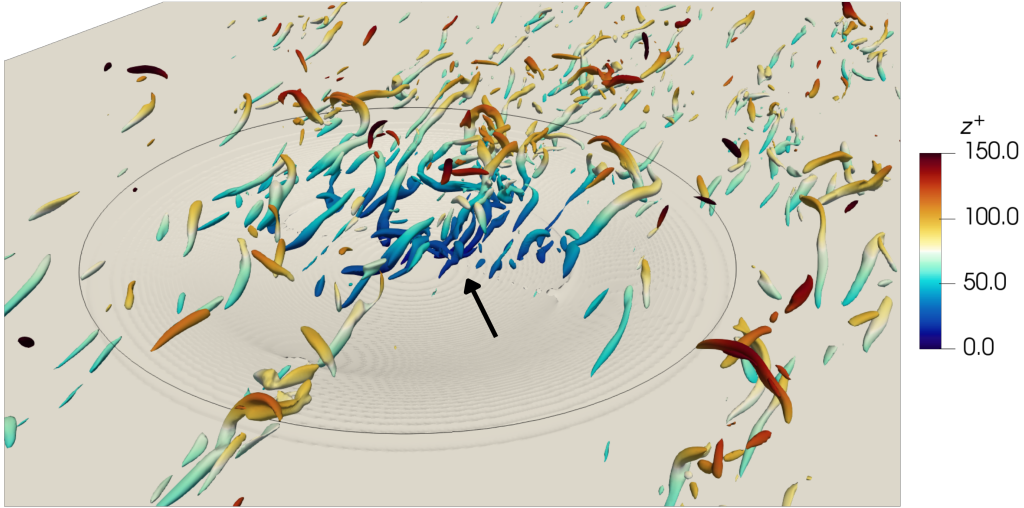


Figure 12: Turbulent vortical structures plotted using isosurfaces of $\lambda_2^+ = -0.04$. The structures are colored using the vertical position z^+ .

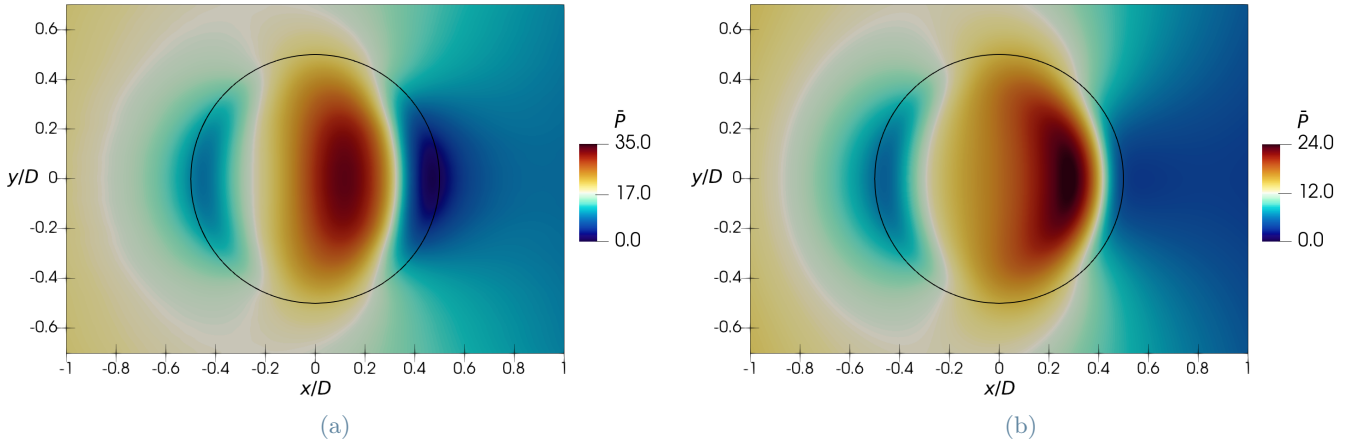


Figure 13: Values of \bar{P} for turbulent (a) and laminar (b) simulations, plotted in the $x - y$ plane at $z = 0.4$.

3.2. Generation of spanwise motion

The importance of the spanwise motion over the recess at the base of the possible drag reduction provided by a dimples array leads to the interest in the study of the mechanism behind its generation. The spanwise momentum balance equation is used, to understand the influence of the different contributions on the evolution of the spanwise velocity for the turbulent and laminar solutions. The equation, written for the turbulent case, reads:

$$\bar{U} \frac{\partial \bar{V}}{\partial x} + \bar{V} \frac{\partial \bar{V}}{\partial y} + \bar{W} \frac{\partial \bar{V}}{\partial z} = -\frac{\partial P}{\partial y} + \frac{1}{Re_\tau} \left(\frac{\partial^2 \bar{V}}{\partial x^2} + \frac{\partial^2 \bar{V}}{\partial y^2} + \frac{\partial^2 \bar{V}}{\partial z^2} \right) - \left(\frac{\partial \overline{u'v'}}{\partial x} + \frac{\partial \overline{v'v'}}{\partial y} + \frac{\partial \overline{v'w'}}{\partial z} \right) \quad (5)$$

with no time derivative being the mean flow stationary. The terms related to the Reynolds stresses, obtain applying the Reynolds decomposition, are not present in the balance for the laminar case.

3.2.1 Laminar solutions

The balance for the laminar flow in the $x - y$ plane over the recess at $z = 0.4$ shows that the main components in the generation of spanwise motion are the pressure gradient (Fig.15a) and the convection due to the streamwise (Fig.14b) and wall-normal directions (Fig.14c). The pressure gradient appears to be the main responsible for the curvature of the streamlines: before the recess and slightly after the leading edge it causes the converging motion of the flow, while, moving inside the indentation, $-\frac{\partial \bar{P}}{\partial y}$ changes sign immediately, first straightening

the streamlines ($-0.4 < x/D < 0$) and then increasing in intensity moving downstream, where the internal pressure grows at the expense of the external one, causing the diverging motion. Just after the recess it changes in sign again, causing the flow to slowly lose the spanwise component. The value of the pressure gradient is more intense in the downstream half of the indentation, where \bar{P} is higher near the center due to the blockage effect (as shown in Fig.13b), resulting in a greater spanwise gradient. It can be observed, moreover, that the peak of $-\frac{\partial \bar{P}}{\partial y}$ on the upstream side of the recess is located at the same y as the opposite one in the downstream half (around $y/D = 0.3$ and $x/D = \pm 0.3$, approximately at the same positions where \bar{V} has its local peaks). The area of the recess that most influences the spanwise motion, in the field above the wall, appears to be included in $0.25 < r/D < 0.5$ (r denotes the distance from the center) in an arc of the circumference drawn between 0 and 45 degrees with respect to the horizontal x axis (this is also the area where the curvature of the streamlines was more intense). The main term that balances the pressure gradient is the streamwise convection (Fig.14b), being almost everywhere the only relevant contribution while, inside the recess near the trailing and leading edge, the wall-normal one (Fig.14c) becomes more important (although its values are one order of magnitude lower than the other two). Hence, we conclude that the \bar{V} component generated is mainly transported downstream, also justifying the asymmetry in x observed in Fig.10b, and a part (although small, being $\bar{W}(\partial \bar{V}/\partial z)$ an order of magnitude smaller than the streamwise component) is transported in the vertical direction. While the convection in z is concentrated inside the recess, in particular to the areas observed before, the one in x continues outside, with opposite sign due to the decreasing value of $\partial \bar{V}/\partial x$, being there the only term to balance the pressure gradient.

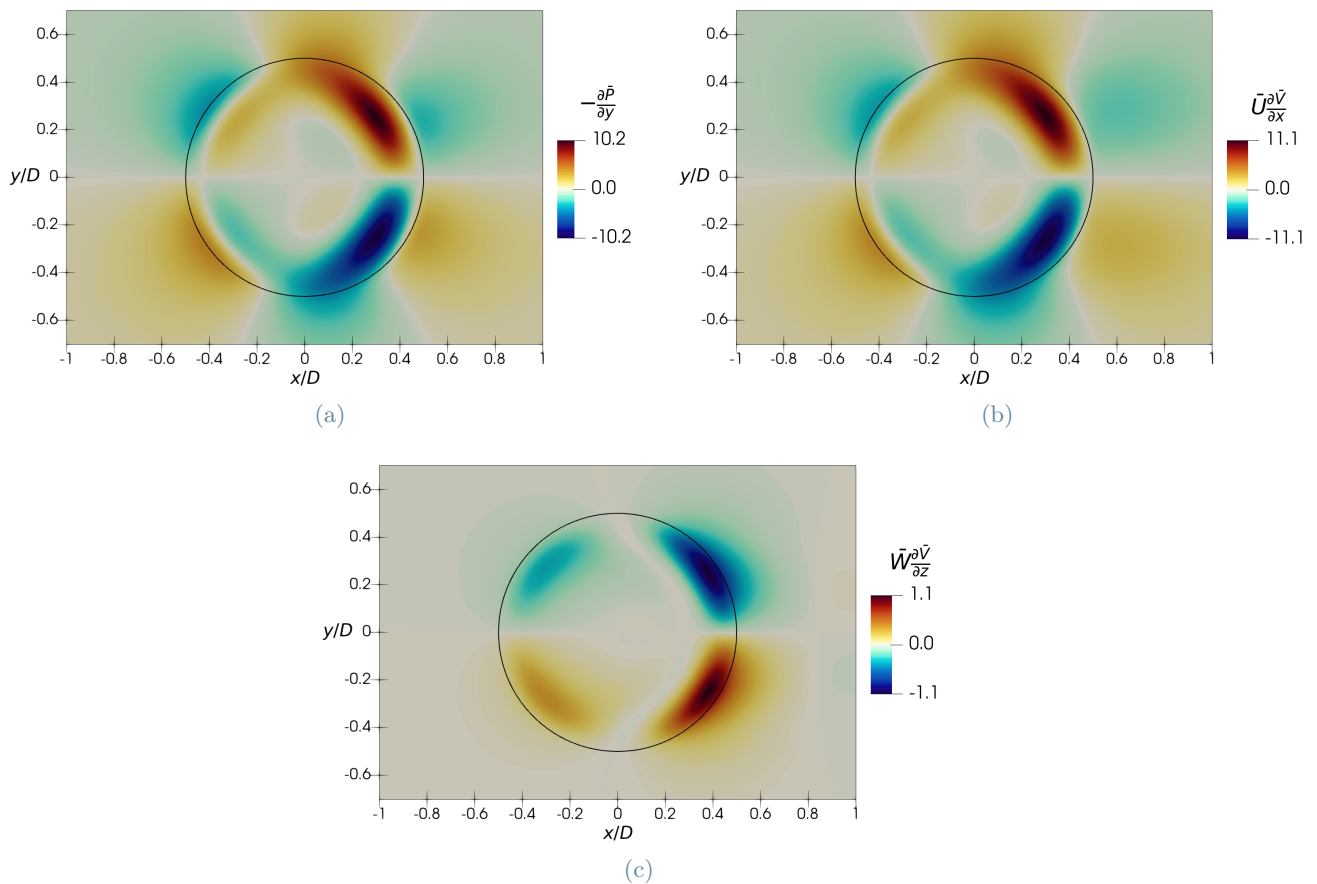


Figure 14: Plot of the pressure gradient and convective term of the momentum balance for \bar{V} , taken in the plane $x - y$ at $z = 0.4$ for laminar solutions. (a) $-\frac{\partial \bar{P}}{\partial y}$; (b) $\bar{U} \frac{\partial \bar{V}}{\partial x}$; (c) $\bar{W} \frac{\partial \bar{V}}{\partial z}$.

The components of equation 5 are then plotted in the $x - z$ plane, taken at $y/D = -0.25$, the one along which the maximum value of \bar{V} was computed, to understand how they are influenced by the wall variation. In addition to the three terms already mentioned, close to the wall, the diffusion in the z direction also assumes importance (Fig.15); the other components, being one or even two orders of magnitude smaller are less relevant and therefore not shown. Upstream of the recess the main contributions come from the pressure gradient, which causes the convergent motion of the flow, the streamwise convection, and, near the wall, the diffusion term. Inside the recess, as observed also in the $x - y$ plane, the value of $-\frac{\partial \bar{P}}{\partial y}$ is almost everywhere negative, and decreases moving in the vertical direction. The influence of the \bar{W} convection and the diffusion term is

concentrated near the wall while everywhere else the pressure gradient is balanced by the streamwise convective term. $\frac{1}{Re_\tau} \frac{\partial^2 \bar{V}}{\partial z^2}$ becomes much more significant in the downstream half, between $x/D = 0.25$ and $x/D = 0.5$, where it is, close to the wall, the main balance of $-\frac{\partial \bar{P}}{\partial y}$.

In conclusion, the principal actors in the generation of spanwise motion are the pressure gradient and the convection in the streamwise direction. The undisturbed flow is curved toward the center of the recess, then, starting from the leading edge, its direction slightly changes from converging to diverging and, downstream of the recess, the effect of the spanwise motion decreases. Near the wall, and up to $z = 0.5$, \bar{V} is convected also in the vertical direction, while the diffusive term acts mainly near the wall, especially in the downstream half, where the velocity gradient in z is greater.

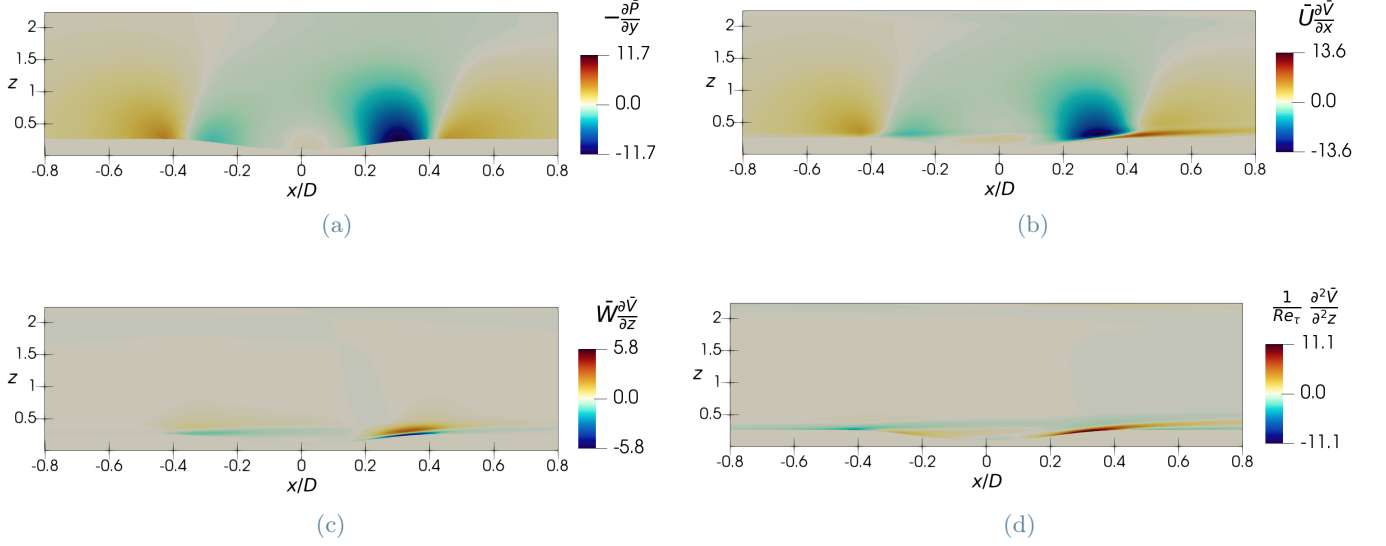


Figure 15: Plot of the pressure gradient, convective and diffusive terms of the momentum balance for \bar{V} , taken in the plane $x - z$ at $y/D = -0.25$ for laminar solutions. (a) $-\frac{\partial \bar{P}}{\partial y}$; (b) $\bar{U} \frac{\partial \bar{V}}{\partial x}$; (c) $\bar{W} \frac{\partial \bar{V}}{\partial z}$; (d) $\frac{1}{Re_\tau} \frac{\partial^2 \bar{V}}{\partial z^2}$.

3.2.2 Turbulent solutions

The most relevant terms of the balance equations for the turbulent solutions are, in both $x - y$ (Fig.16) and $x - z$ planes (Fig.17) the same found for the laminar case, with the addition of two terms due to the turbulent fluctuations $-\frac{\partial v'v'}{\partial y}$ and $-\frac{\partial v'w'}{\partial z}$. Only the most relevant contributions are shown.

The results (Fig.16) are qualitatively very similar to those obtained in the laminar case. Nevertheless the values of the pressure gradient (Fig.15a) upstream are more intense than the laminar ones, meaning that the streamlines are made to curve earlier and more abruptly, while in the downstream half higher values are reached closer to the center and are more extended inside the recess. The sign of the pressure gradient changes at the trailing edge, meaning that the streamlines are straightened already when exiting the indentation: their bending at the recess exit is again stronger than the laminar one, following the greater curvature at the trailing edge. The similarities between the two solutions can be observed also in the streamwise (16b) and wall-normal convection (16c) although the values in the latter are almost four times the laminar ones. Also in the $x - z$ plane (Fig.17) the results are qualitatively very close, although slightly higher values of pressure gradient are reached near the wall (Fig.17a). The streamwise (Fig.17b) and wall-normal (Fig.17c) convection presents the same behavior than the laminar counterpart with higher values, especially near the wall, while the diffusive term (Fig.17d) is slightly different since, besides having a larger range, it assumes a greater importance already at the recess center, being positive along all its span. From the components related to turbulent fluctuations the most relevant ones are $-\frac{\partial v'v'}{\partial y}$ (Fig.17e) and $-\frac{\partial v'w'}{\partial z}$ (Fig.17f) which influence become important only in the upstream half of the recess, near the wall. They present opposite signs and the one corresponding to the vertical direction is slightly higher and has, very close to the wall in the downstream half, a negative area caused by the non-penetration condition.

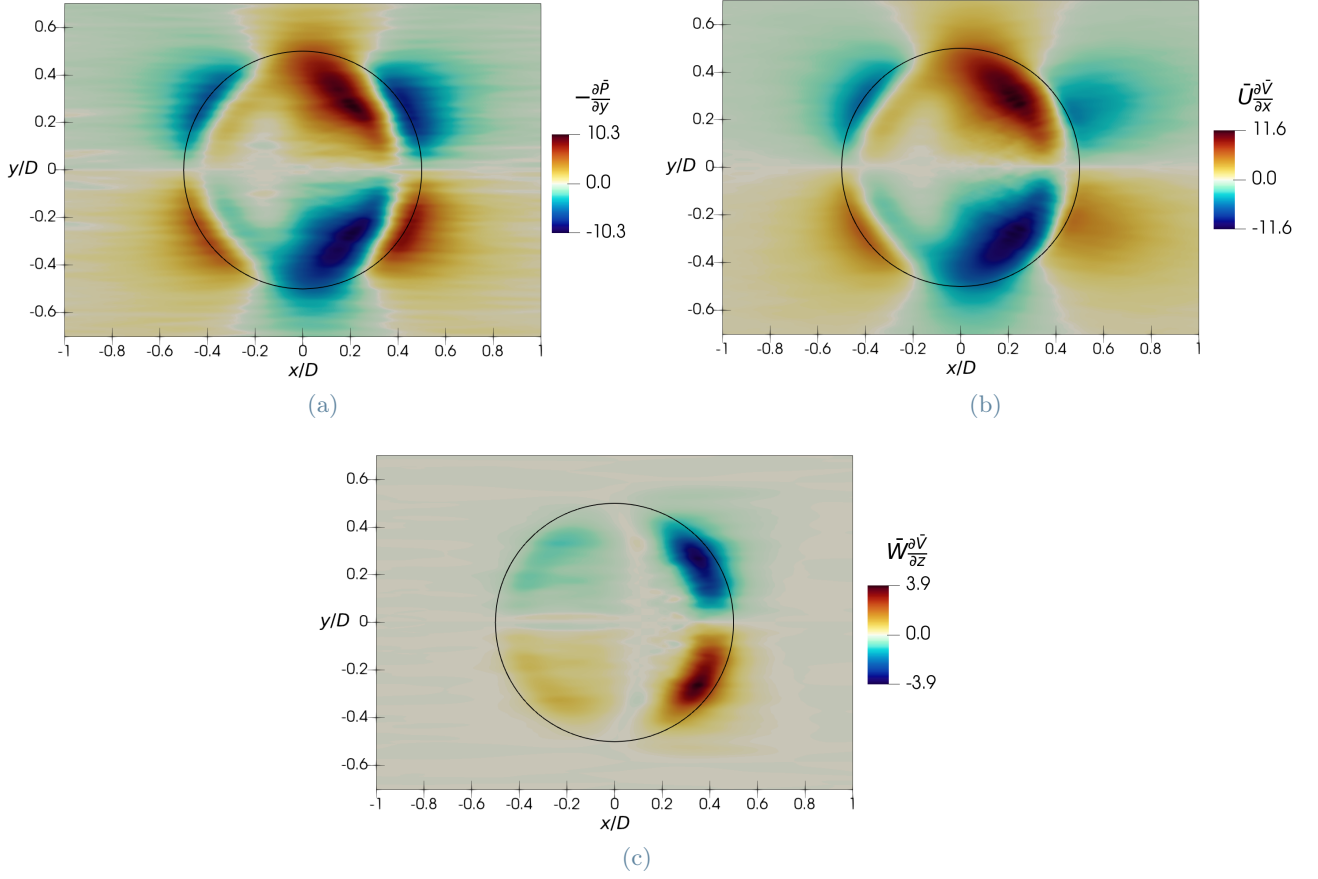


Figure 16: Plot of the pressure gradient and convective term of the momentum balance for \bar{V} for the turbulent solutions, taken in the pane $x - y$ at $z = 0.4$. (a) $-\frac{\partial \bar{P}}{\partial y}$; (b) $\bar{U} \frac{\partial \bar{V}}{\partial x}$; (c) $\bar{W} \frac{\partial \bar{V}}{\partial z}$.

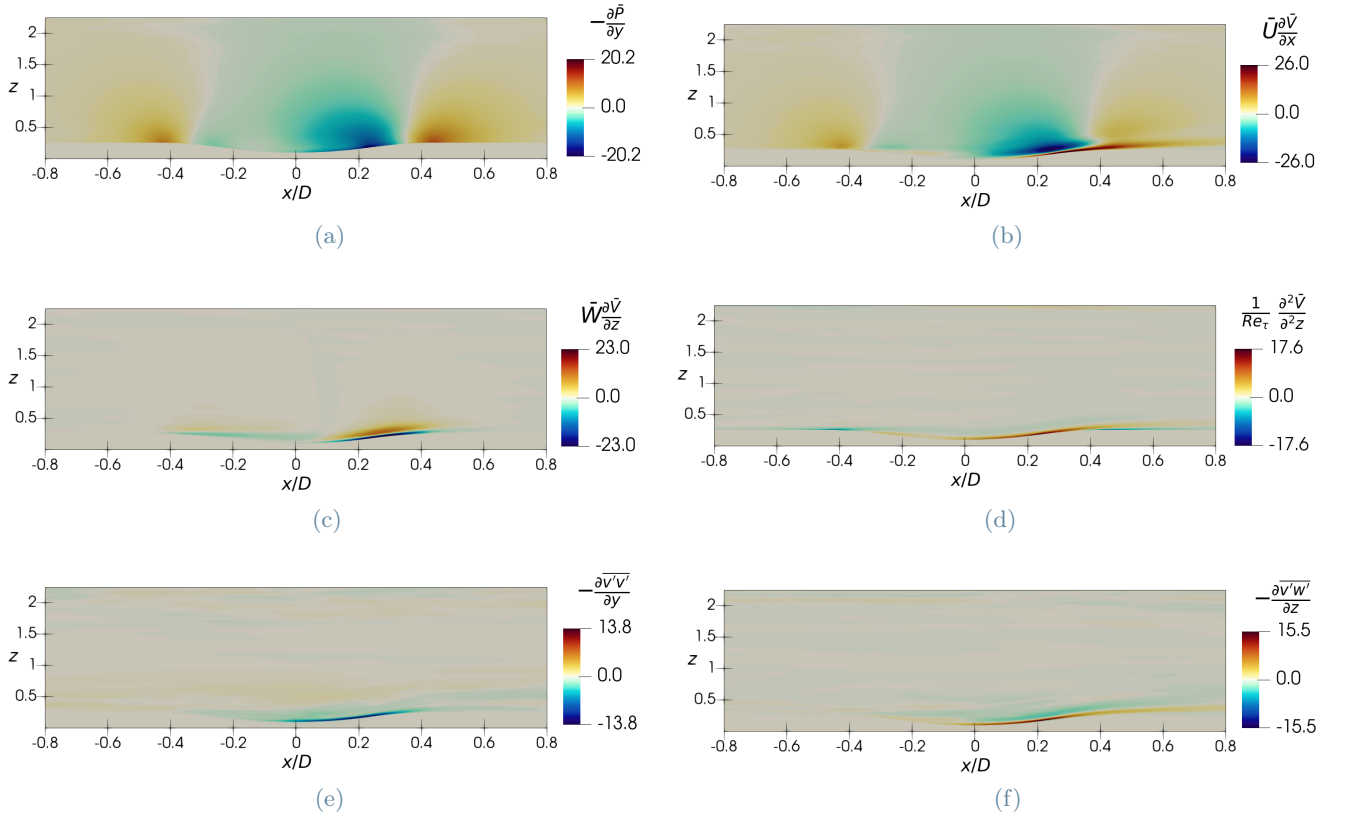


Figure 17: Plot of the pressure gradient, convective, diffusive and Reynolds stresses terms of the momentum balance for \bar{V} for the turbulent solutions, taken in the pane $x - z$ at $y/D = -0.25$. (a) $-\frac{\partial \bar{P}}{\partial y}$; (b) $\bar{U} \frac{\partial \bar{V}}{\partial x}$; (c) $\bar{W} \frac{\partial \bar{V}}{\partial z}$; (d) $\frac{1}{Re_\tau} \frac{\partial^2 \bar{V}}{\partial z^2}$; (e) $-\frac{\partial \overline{v'v'}}{\partial y}$; (f) $-\frac{\partial \overline{v'w'}}{\partial z}$.

3.3. Skin friction

Following what is stated in [15] the streamwise component of the wall friction (τ_w) and pressure drag (P_d) is considered, since the interest is to study the drag resultant in the direction of the mean flow. They are defined as:

$$\tau_w = \nu \frac{\partial \bar{U}_{//}}{\partial n} \hat{x} \quad (6)$$

$$P_d = \bar{P} \hat{n}_x, \quad (7)$$

where $\bar{U}_{//}$ is the component of the velocity vector tangent to the wall, \hat{x} indicates that the wall friction is taken in streamwise direction, $\partial/\partial n$ is the derivative in wall-normal direction and \hat{n}_x is the unit vector normal to the wall projected in x and. Their integration over the surface leads to the total skin friction and pressure drag respectively and reads:

$$D_f = \int_{A_w} \tau_w dA_w, \quad (8)$$

$$D_p = \int_{A_w} P_d dA_w, \quad (9)$$

with A_w the wall surface, chosen as a portion of the total surface i.e. $[x/D; y/D] = [-0.8; 0.6; -0.5; 0.5]$. The dimensions of A_w are used to capture in the integration the main contribution of the recess on the mean flow since, as it will be observed in the following, the effects of the recess on skin friction and pressure drag are mainly concentrated inside its radius.

Figures 18a and 18b show the distribution of τ_w over the recess for the turbulent and laminar solutions, while 18c plots their values as a function of the streamwise position x at different y/D . Because of the adimensionalization choices made, the reference value is $\tau_w = 1$ on the flat surface (for both cases). The negative area, contoured by the white isoline in 18a and 18b for $\tau_w = 0$, highlights the recirculation region: it is again observed that for the laminar case its extension is greater in x than the turbulent one, while is quite similar in y , being limited between $y/D = \pm 0.25$. The variation of the skin friction in the streamwise direction for the turbulent case can be linked with the behavior of the mean velocity observed in §3.1. Three main regions are observed:

- $x/D < -0.45$. The wall friction starts to slightly increase approaching the edge of the recess, from the reference value of 1 up to ≈ 1.3 (a 30% increase) at $y = 0$. This can be linked both to the slight variation in the $\bar{U}(z)$ profiles in this area and to the increase of wall-normal velocity that was observed at $x/D = -0.6$ (Fig.8a).
- $-0.45 < x/D < 0.1$. The wall friction decreases, following the decrease in the slope of $\bar{U}(z)$ computed near the wall moving to the center. Although the presence of \bar{W} gives a positive contribution to the local value of τ_w , its value is still too small to balance the reduction of $d\bar{U}/dz$. This variation of τ_w appears to be gentler moving in the y direction to the edge of the recess, a straightforward consequence of the increase of the \bar{U} slope (Fig.5b) moving from the center to the edge in the spanwise direction. The negative area corresponds to the separation region.
- $x/D > 0.1$ The wall friction increases moving downstream, reaching to the maximum value located at $x/D \approx 0.35$ and again the variation of τ_w is gentler moving in span towards the recess edge. The wall friction returns to the flat wall value just after the end of the recess and the effects of the indentation is perceived up to $x/D \approx 0.7$.

Comparing the results of the turbulent case with the laminar solutions (dashed lines in Fig.18c) it can be observed that the values of τ_w are very close for the two cases up to $x/D = -0.25$, slightly after the occurrence of the separation. Moving downstream, the dashed lines present lower values, reaching their maximum slightly after the turbulent solutions (at $x/D \approx 0.45$). Near the trailing edge the laminar wall friction decrease is slower, becoming consequently larger than the turbulent one, which decreases faster from its peak to the reference flat value. The separation of different extents certainly affects the wall friction trend. However the same behavior is observed, i.e. similarity of results in the upstream half of the recess up to about $x/D = -0.25$, also in the τ_w at the lateral edge ($y/D = -0.5$) and at $y/D = -0.25$ at the limit of the separation.

Integrating τ_w over the surface A_w (defined above) a value of $D_f \approx 0.948$ for the turbulent case is obtained, equivalent to a 5% decrease in the total friction drag with respect to the flat wall. For the laminar solutions, as a consequence of the general lower values of skin friction, the computed value is $D_f \approx 0.815$, giving the, predictable, conclusion that for a single recess the laminar skin friction is lower than the turbulent one, also because of the greater separation that the former presents.

Having compared the turbulent results with the laminar ones, some questions on the influence of the turbulent

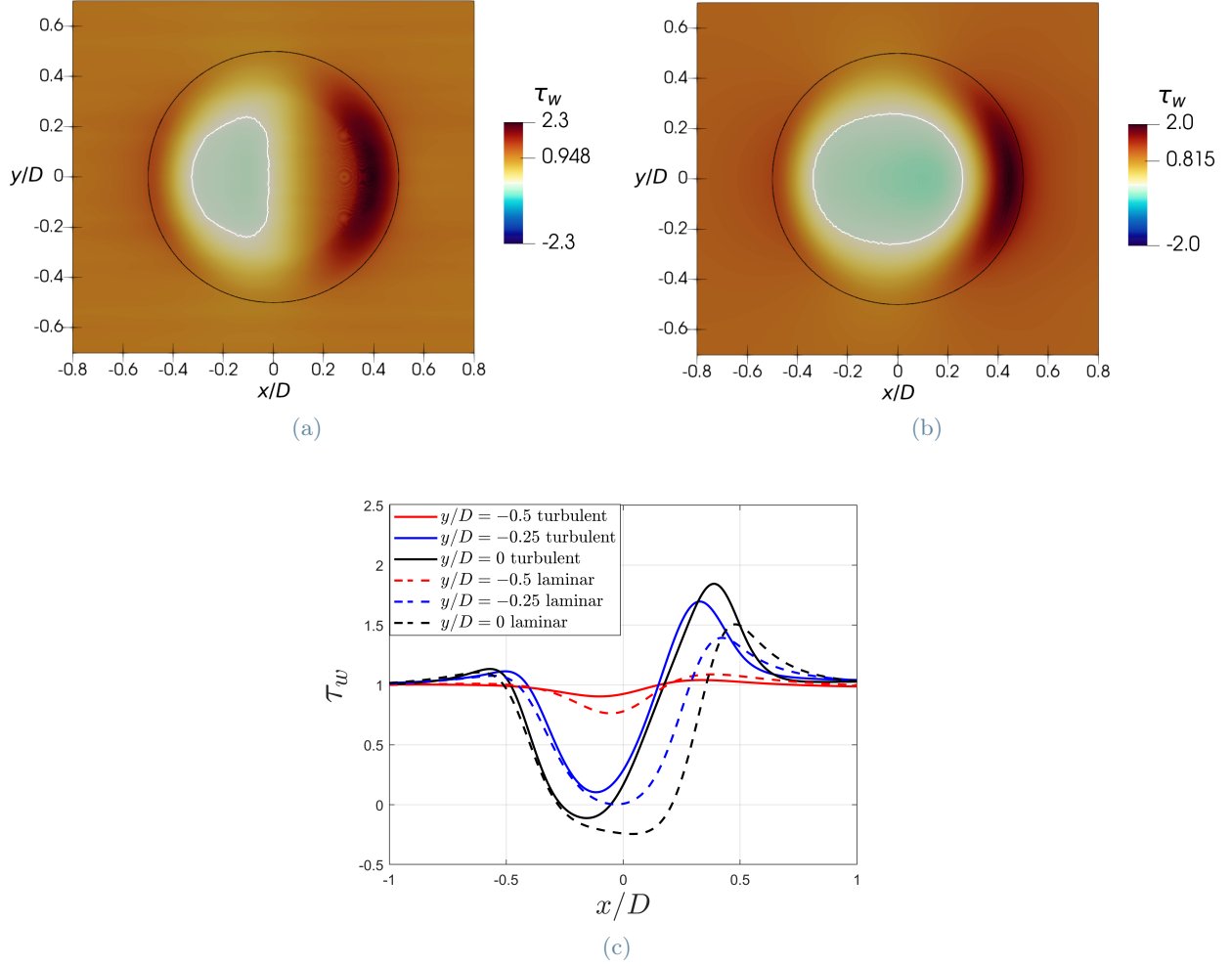


Figure 18: Wall friction τ_w over the recess. The total friction drag D_f is marked in the label for both (a) turbulent $D_f \approx 0.948$ and (b) laminar $D_f \approx 0.815$ case. The black circle indicates the recess and the white line is the isoline at $\tau_w = 0$. (c) Plot the values of skin friction of the laminar (dashed line) and turbulent (solid line) along x for different values of y/D .

properties on skin friction remain open. In incompressible flows, turbulent friction directly depends on the mean velocity only, and the link with the turbulent properties is the turbulent kinetic energy production, which represents the transfer of energy from the mean flow to the turbulence. A decomposition based only on the shear stress is meaningless since its contribution to the skin friction drops to zero while integrating over the wall, so, to have a better visualization of the various influences on the wall friction, a variation of the FIK (Fukagata-Iwamoto-Kasagi [6]) decomposition was implemented on the turbulent results.

3.4. Influence of turbulent properties on skin friction

3.4.1 Derivation of the skin friction decomposition

The so-called FIK decomposition, developed by Fukagata et al.[6], allows to obtain an analytical expression for the constituent contributions of skin friction in a turbulent flow, that relates the turbulence-induced excess friction to the Reynolds shear stress weighted by a linear function of the wall distance. Being the original FIK formerly limited to canonical cases with two-dimensional mean flow, a variation of the decomposition applicable over the recess was developed, following the extensions for non-planar walls proposed by [2] and [16]. The derivation of the identity starts from the evolution equation for the mean streamwise momentum for an incompressible flow that, after applying the Reynolds decomposition, reads:

$$\frac{\partial \bar{U}}{\partial t} + \bar{U}_i \frac{\partial \bar{U}}{\partial x_i} = -\frac{\partial \bar{P}}{\partial x} + \frac{1}{Re_\tau} \frac{\partial^2 \bar{U}}{\partial x_i \partial x_i} - \frac{\partial \overline{u'_i u'_i}}{\partial x_i} \quad (10)$$

where \bar{U}_i indicates a generic component of the mean velocity and x_i is a generic direction. Applying the hypothesis of stationarity the time derivative of the mean flow drops to zero. Gathering the terms with the same derivatives and making them explicit the following equation is obtained

$$\bar{I}_x + \frac{\partial \bar{P}}{\partial x} = \frac{\partial}{\partial y} \left(\frac{1}{Re_\tau} \frac{\partial \bar{U}}{\partial y} - \overline{u'v'} \right) + \frac{\partial}{\partial z} \left(\frac{1}{Re_\tau} \frac{\partial \bar{U}}{\partial z} - \overline{u'w'} \right) \quad (11)$$

$$\text{where } \bar{I}_x = \bar{U}_i \frac{\partial \bar{U}}{\partial x_i} - \frac{1}{Re_\tau} \frac{\partial^2 \bar{U}}{\partial x^2} + \frac{\partial \overline{u'w'}}{\partial x}$$

Following the same procedure used in [6] and [2] a triple integration is performed on Eq.11. Since the geometry is not homogeneous in the spanwise direction the inner integration is computed over the two-dimensional cross-section $\Sigma(x)$ (similarly to what was done by [16]), normal to the streamwise direction, which extends arbitrarily between two points in y and from the lower wall up to a generic height z_{top} , while the other two are performed in the z -direction, the first up to a generic z and the last up to z_{top} . The cross-section $\Sigma(x)$ is built in y direction between the same point used for the integration of the complete skin friction drag, i.e. between $y/D = -0.5$ and $y/D = 0.5$, while z_{top} was put equal to the channel half height that is, in the Cartesian reference frame with the origin on the lowest point in the wall, $z = 1.25$. The three boundary conditions used are non-slip conditions on the wall ($\bar{U} = \bar{V} = \bar{W} = 0$), symmetry in spanwise direction and $\frac{\partial \bar{U}}{\partial z} = 0$ at $z = z_{top}$ (which is an approximation but was adopted also by [16]). The resulting identity, which depends only on the streamwise position x , having lost direct information on the spanwise direction through the integration over $\Sigma(x)$, is

$$\begin{aligned} \tilde{\tau}_w(x) = & \frac{2}{h(x)^2} \frac{1}{\alpha(x)} \frac{1}{Re_\tau} \iint_{\Sigma(x)} \bar{U} \frac{d\Sigma}{L_y} \quad (\tau_{lam}) \\ & + \frac{2}{h(x)^2} \frac{1}{\alpha(x)} \iint_{\Sigma(x)} (h-z) \overline{(-u'w')} \frac{d\Sigma}{L_y} \quad (\tau_{turb}) \\ & + \frac{2}{h(x)^2} \frac{1}{\alpha(x)} \iint_{\Sigma(x)} \frac{1}{2} (h-z)^2 \left(\bar{I}_x + \frac{\partial \bar{P}}{\partial x} \right) \frac{d\Sigma}{L_y} \end{aligned} \quad (12)$$

where $\tilde{\tau}_w(x)$ is the skin friction averaged in spanwise direction. $\alpha(x)$ is the normalization coefficient for complex surfaces, equal to

$$\alpha(x) = \int_{\partial \Sigma(x)} \left(1 - \frac{z_{wall}(x, l)}{z_{top}} \right)^2 \sqrt{1 - (\hat{n}_x)^2} \frac{dF_x}{F_x} \quad (13)$$

with $\partial \Sigma(x)$ the curve at the wall of $\Sigma(x)$, $F_x = L_y \tilde{\tau}_w(x)$, $dF_x = \tau_w dl$ (l coordinate along the wall in spanwise direction) and z_{wall} the local wall height. $h(x)$ is the distance between z_{top} and the wall, mediated in y at each streamwise position, while L_y is the distance between $y/D = -0.5$ and $y/D = 0.5$. \hat{n}_x is the unit vector normal to the wall projected in x , the same used in equation 7. The three terms of equation 12 can be defined, respectively, as the "laminar", "turbulent" and "spatial heterogeneity" contributions, although, unlike in the classic FIK formulation, no adimensionalization is performed and the identity is referred directly to the skin friction, instead of the friction coefficient. In contrast with the original formulation the identity does not provide the exact results for a flat wall, since it was derived from the direct integration of the streamwise momentum balance, to take into account with the integration domain the non-planar and non-homogeneous wall, while the original decomposition for channel flows requires some previous modifications to the balance equation. This choice was dictated also by the observation that the results, and their physical meaning, are strictly connected to the adimensionalization choices, the reference height and the domain of integration, as well as the mathematical manipulations that allow to obtain the identity [2]. The direct integration of the momentum balance equation to obtain terms dependent only on the mean velocity and Reynolds shear stresses, without adimensionalization of the results, allowed to stay in the most general case also for a non-planar geometry, gaining insight into the relative influence of the various components on the skin friction along the recess extension, being able to account for the wall geometry and avoiding to lose information while manipulating the equations. Although the values provided are not the exact ones on the flat wall, the ratios between the laminar and turbulent terms are the same obtained with the classic FIK decomposition, meaning that the errors are only quantitative and the formulation leads to qualitative correct results.

3.4.2 Application of the FIK decomposition

Figure 19 shows the comparison between the averaged wall friction in spanwise direction $\tilde{\tau}_w(x)$ and the laminar and turbulent contribution on the friction computed with the FIK decomposition (scaled on their respective flat wall value to obtain τ_{lam} and τ_{turb} equal to 1 upstream of the recess for a better comparison). While these two terms are computed using Eq.12, the heterogeneity one was obtained by subtracting the others

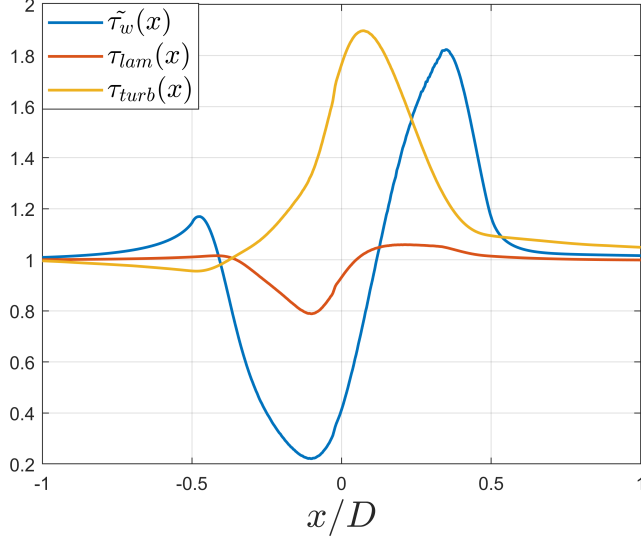


Figure 19: Plot of $\tilde{\tau}_w(x)$ and the laminar and turbulent contribution to the skin friction computed through the FIK decomposition. These last two are scaled in order to have the same value of $\tilde{\tau}_w(x)$ on the flat wall for a better visualization.

from the computed skin friction. It is important to specify that, precisely because of the choice made for the adimensionalization, this third term contains most of the errors linked to this approximation, thus the discussion is focused on the first two, and this last one is not plotted. The first term depends on the streamwise mean velocity while the turbulent one on the $\overline{u'w'}$ component of the Reynolds shear stress only, since $\overline{u'v'}$ cancels out during the integration. It has to be specified that the linear weighting function that multiplies $\overline{u'w'}$ has been contested by some authors, like [21], who stated that, although derived mathematically from the integration of Eq.11, it doesn't have a simple explanation in terms of physical processes. This is true especially along a recess, which presents a strong non-linearity of its phenomena in wall-normal direction.

In the upstream half the laminar contribution decreases, following the decrease in the slope of $\bar{U}(z^+)$ observed in Fig.6a, while it increases downstream, where the slope of $\bar{U}(z^+)$ is steeper. Overall, τ_{lam} appears to cause mainly a drag reduction, assuming values lower than the relative ones on the flat wall. On the other hand the turbulent term is almost everywhere greater than the correspondent flat wall values, increasing while moving inside the recess, especially in the downstream half. It can be compared with the distribution of $\overline{u'w'}$ shown in Fig.20, where it is plotted in the $x - z$ plane at $y/D = 0$. The increase of τ_{turb} in the downstream half corresponds to the increase in Reynolds shear stress, which reaches the maximum slightly after $x/D = 0$, where the wall begins to climb. The influence of the recess on the $\overline{u'w'}$ is perceived up to $x/D = 0.8$, as can be observed also in the value of the turbulent contribution outside the indentation, which remains higher than the correspondent flat value. Finally in the downstream half of the recess, close to the wall, a change in the value of $\overline{u'w'}$ that becomes positive is observed, probably caused by the non-penetration condition.

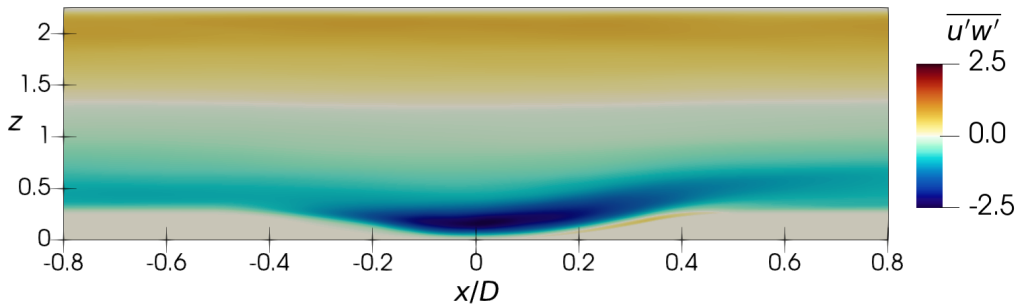


Figure 20: Plot of the Reynolds shear stress $\overline{u'w'}$ along the $x - z$ plane at $y = 0$.

In Fig.21 $\tilde{\tau}_w(x)$ for the turbulent case is plotted against the correspondent laminar skin friction averaged in span. As observed also in Fig.18c in the upstream half, up to $x/D = -0.1$, the results for both flows are very similar, whereas moving in the downstream part $\tilde{\tau}_w(x)$ turbulent grows faster than the laminar one, reaching its maximum value already at $x/D \approx 0.3$. $\tilde{\tau}_w(x)$ laminar remains instead lower until $x/D \approx 0.1$, where it increases

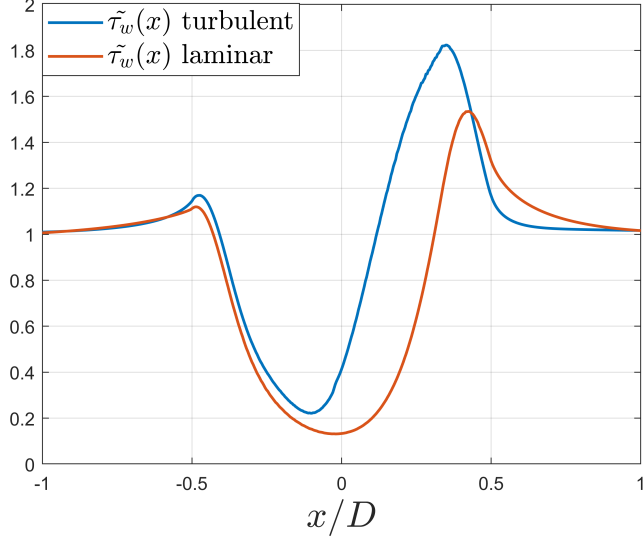


Figure 21: Plot of $\tilde{\tau}_w(x)$ for the turbulent and laminar simulations.

more gently up to $x/D = 0.4$. The discrepancy between the laminar and turbulent case is concentrated mainly in the second half of the recess, where, from the application of FIK (Fig.19), the greatest influence of the turbulent component $\overline{u'w'}$ in the wall friction is observed. This indicates that the higher value of $\tilde{\tau}_w(x)$, as well as the more abrupt variation from $x/D \approx -0.1$ to $x/D \approx 0.3$, may depend on the increase of the Reynolds shear stress, which is absent in the laminar case. The decrease of $\tilde{\tau}_w(x)$ turbulent below the laminar counterpart at $x/D \approx 0.5$ (Fig.21 and 18c) is not straightforward looking at Fig.20. It is instead useful to consider the values of the turbulent kinetic energy (TKE) production along the recess (Fig.22), since, as stated before, this is the main relation between the skin friction and the turbulent intensity. The TKE is defined as $k = 1/2(\overline{u'u'} + \overline{v'v'} + \overline{w'w'})$ and its production $P_{TKE} = -\overline{u'_i u'_j} \partial \overline{U}_i / \partial x_j$, where $\overline{u'_i u'_j}$ indicates a generic component of the Reynolds stresses, \overline{U}_i and x_j a generic mean velocity and a direction. The first half of the dimple presents the peak of production, over the separation bubble and where $d\overline{U}/dx$ decreases (Fig.5), and corresponds to the decrease in skin friction observed in Fig.21. In the downstream half, instead, P_{TKE} reduces and this is matched by the increase of $\tilde{\tau}_w(x)$. At $x/D = 0.4$, at the peak of skin friction, where the vertical variation of the mean velocity is greater, a negative production value is present, related to a positive $d\overline{U}/dx$ caused by the wall curvature. Instead, the decrease of $\tilde{\tau}_w$ turbulent, even below the equivalent laminar value, observed between $0.4 < x/D < 0.5$, can be linked to the increase of P_{TKE} in the vicinity of the wall (Fig.22, pointed by the arrow) due to the negative value of $d\overline{U}/dx$ see in Fig.5, i.e. where the flow decelerates, near the surface, moving outside the recess.

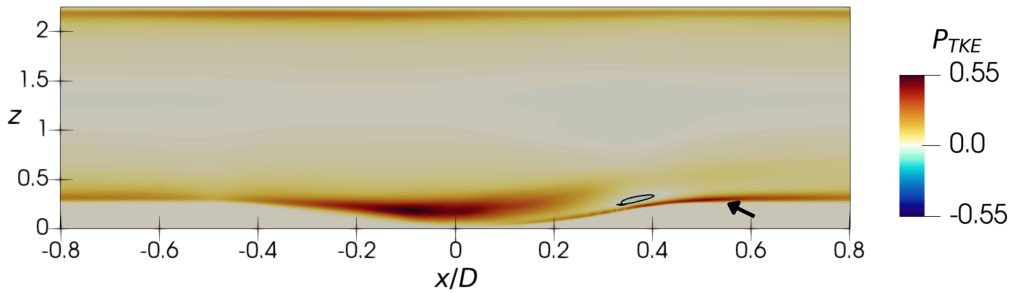


Figure 22: Plot of the TKE production, plane $x - z$ at $y = 0$. The isline in black highlights the negative value of P_{TKE} .

3.5. Pressure drag

Unlike skin friction, pressure drag is a phenomenon completely absent on a flat surface, that arises due to the geometry of the recess. This means that its presence cannot bring any positive contribution to the reduction of total drag but, on the contrary, can only worsen the performance of a dimples array. Figure 23 pictures the

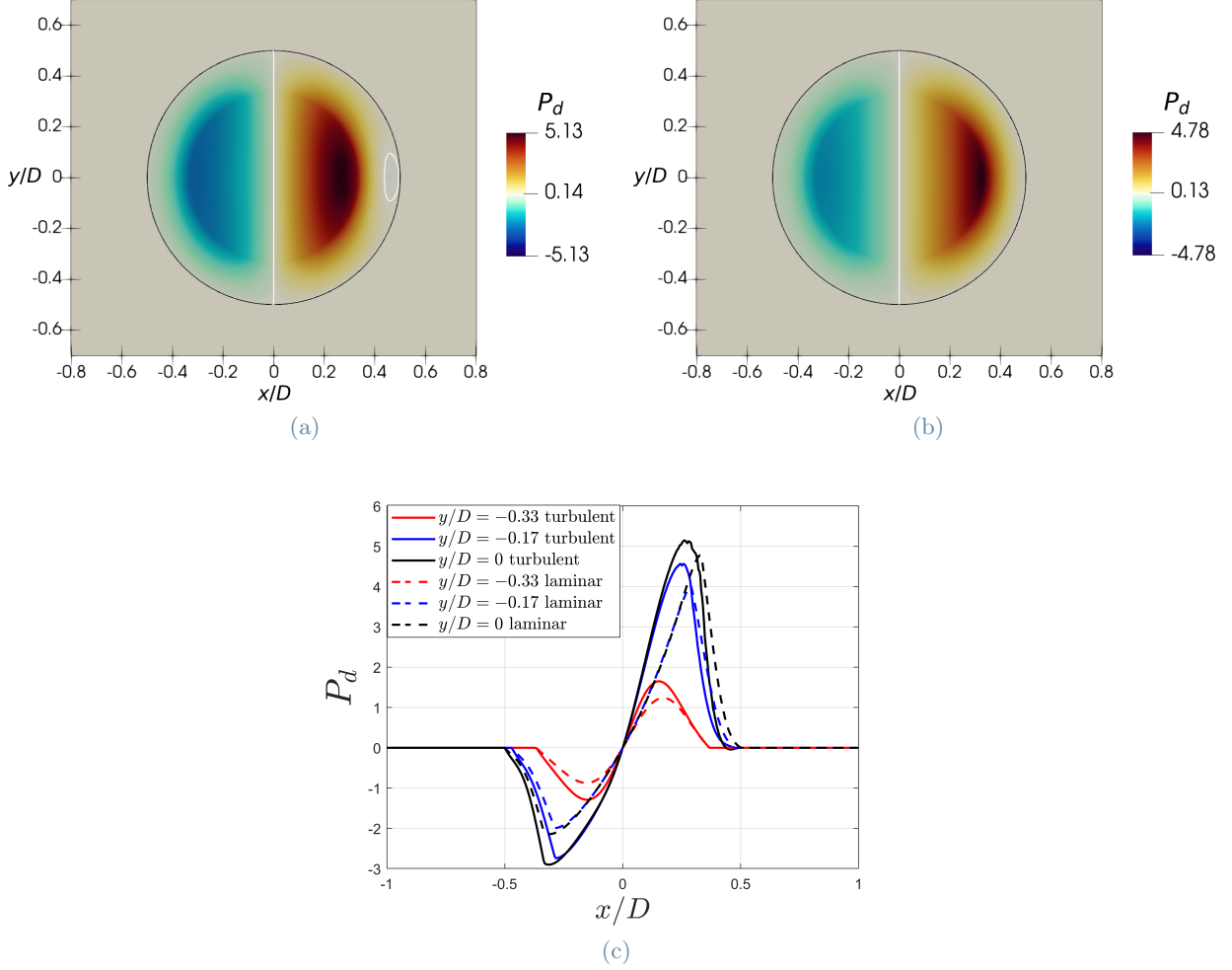


Figure 23: Pressure drag over the recess. The total pressure drag D_p is marked in the label for both (a) turbulent $D_p \approx 0.14$ and (b) laminar $D_p \approx 0.129$ case. The black circle indicates the recess while the white line is the isoline for $P_d = 0$. (c) Plot the values of pressure drag along x for different values of y/D .

distribution of the pressure drag over the recess for the turbulent and laminar solutions. The drag is negative everywhere in the upstream half whereas it's positive in the downstream one for both cases, with the exception of the trailing edge at $y/D = 0$ for the turbulent one (Fig.23a), where P_d becomes slightly negative, being the local pressure below zero (i.e below the outlet value which was used as a reference and put to zero). The values reached in the first half of the recess are less intense than the ones on the downstream side, as a consequence of the pressure distribution (3.1) which has its peak just before the trailing edge, near the wall slope increase. The results for the laminar solutions (Fig.23b) present the same behavior but with smaller values: the negative contribution on the trailing edge is, however, absent, since the drop in the pressure computed at the end of the recess doesn't go below zero. Lastly looking at Fig.23c, where the pressure drag for the two solutions is plotted along x for different y/D , it can be observed that P_d for the turbulent case has the peaks closer to the center and presents, from $x/D = 0.3$, a steeper variation than the laminar case for y closer to the center, probably because of the greater acceleration to which their flow is subjected, forcing the streamlines to curve more when moving outside the recess, as a result of the higher speeds achieved within the indentation. The variation is instead the same near the lateral edges.

Integrating the solutions over the same area A_w used for the friction drag, the values obtained are $D_p \approx 0.14$ for the turbulent case and $D_p \approx 0.13$ for the laminar one. Decreasing the recess depth would lead to a reduction of the vertical area projected in the x direction and, consequently, a minor pressure drag: this is consistent with the idea that dimples array made by shallower recesses lead to better drag performances [8]. Another way to control the pressure drag could be the change in the downstream wall slope, leading to a minor increase in the local pressure.

Figure 24 pictures the local drag variation $\Delta D\%$, computed between the total drag of the dimple, obtained

by summing the skin friction and pressure drag, and the reference flat wall friction for both the turbulent and laminar solutions, namely $\Delta D\% = ((\tau_w + P_d) - 1)\%$, being the drag on the flat reference wall equal to 1 because of the adimensionalization choices. For the turbulent case, plotted in Fig.24a, the upstream half of the recess causes a drag reduction, where both τ_w and P_d carry a positive contribution, whereas their values increase moving downstream. Although τ_w is initially lower than the flat wall friction the negative contribution brought by the pressure drag immediately results in a deterioration of the $\Delta D\%$. The same considerations can be made for the laminar solutions (Fig.24b), where, however, the values of $\Delta D\%$ are smaller.

Integrating the total drag ($\tau_w + P_d$) over the recess (on A_w defined above) the result is $(D_f + D_p) \approx 1.09$ for the turbulent solutions, resulting in a total variation $\Delta D_{tot}\% = ((D_f + D_p) - 1)\% \approx 9\%$ (w.r.t the flat wall). With the same recess geometry disposed into an array, Ng in 2020 [15] obtained a $\Delta D_{tot}\% \approx 6.4\%$. The difference between the two values can bring some considerations: first, the mutual interaction among the recesses, not considered in the present study, could lead to a change in the total values of D_f and D_p , since in a dimpled array the spanwise velocity interact between adjacent recesses, leading an inevitable change in the local skin friction; second, the differences could be explained by the different computational method used and third, it could depend on the volume chosen for the definition of the Reynolds number and the pressure drop over the recess, as stated in section §1 and [8]. Integrating the total drag for the laminar case $\Delta D_{tot}\% \approx -5.6\%$ is obtained, showing that for the laminar flow the recess alone provides a slight drag reduction.

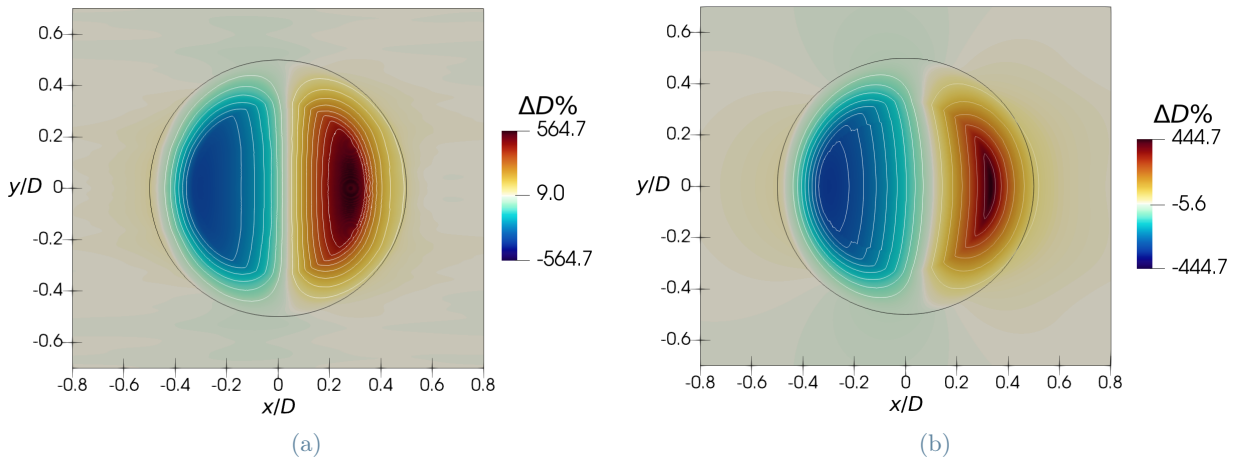


Figure 24: $\Delta D\%$ over the recess. The total drag variation ΔD_{tot} is marked in the label for both (a) turbulent $\Delta D_{tot}\% \approx 9\%$ and (b) laminar $\Delta D_{tot}\% \approx -5.6\%$ case. The recess is represented in the plot by the black circle and the isolines at different values of drag are plotted in white.

4. Discussion and conclusions

The turbulent flow over a circular recess was characterized, to understand the recess influence on the flow behavior and its ability to generate a spanwise motion. The simulations are compared to the laminar counterpart, to discern whether the laminar flow alone provides significant explanations of the phenomena and how they are influenced by the turbulent properties. This study follows the idea proposed by some authors [30, 33] that several recesses, disposed into an array, may induce a motion of the near wall flow similar to the spanwise forcing methods, passively providing drag reduction. Being, however, the results on recesses arrays very unclear in the literature, this work focused on an isolated geometry, to learn information on the flow properties and design a recess that could, indeed, lead to a drag reduction. The spanwise component of the mean velocity over the recess presents a converging-diverging pattern, with an asymmetry in the streamwise direction that can be associated with the convection caused by the streamwise current. Its values are higher in the downstream half than in the upstream one, meaning that the diverging motion is stronger than the converging one. A similar behavior is present in the laminar solutions, where the streamwise asymmetry is even stronger. The influence of the recess on the spanwise motion is not limited inside its span but extends for more than one radius upstream and downstream in the flow and in the spanwise direction. Given the importance of the mechanism behind the evolution of spanwise velocity, the momentum balance equation in the spanwise direction for the turbulent and laminar solutions was studied. The two main contributions are, for both simulations, the pressure gradient and the streamwise convection, which balance each other almost everywhere in the flow. Near the trailing edge the wall-normal convection becomes more relevant, in particular for the turbulent case, in which it assumes much higher values than the ones in the laminar solutions. Looking instead at the other two mean velocity

components a separation at the trailing edge is found, more extended in the laminar than in the turbulent case, although for both it remains limited within the recess. Unlike the spanwise component, the streamwise and wall-normal velocities are not particularly influenced in the spanwise direction outside the recess, although the variation of the latter is perceived up to the opposite wall of the channel. Finally the skin friction (τ_w) and pressure drag (P_d) were studied, looking for the area of the recess that provides more drag increase. The skin friction distribution presents very similar values for the turbulent and laminar cases in the upstream half, while they appear quite different in the downstream one. The difference in the results between the two solutions seems to be related to an increase of the Reynolds shear stress in the downstream half of the recess for the turbulent case, pictured using a variation of the FIK (Fukagata-Iwamoto-Kasagi) decomposition for non-planar walls. This decomposition allowed us to obtain a qualitative indication of the relative influence of the mean velocity and Reynolds shear stress in the skin friction. Moreover the turbulent kinetic energy production was compared with the variation of τ_w , showing the relation between an increase in production, that drains energy from the mean flow, with a decrease in skin friction and vice versa. The study of the total drag highlighted that the upstream half of the recess is the one that provides a reduction in drag, while the increment is concentrated on the downstream side where higher values are reached, resulting in a total drag increase for the turbulent flow over the recess when compared to the skin friction over the flat wall.

A homogeneity in the spanwise velocity is necessary to achieve the same mechanism as the spanwise forcing methods. However, as observed looking at the momentum balance, the main term behind the generation of spanwise motion is the pressure gradient that, given the geometry of the recess, will always provide a converging-diverging motion ruining the spanwise homogeneity. What can be achieved, instead, is a local uniformity, obtained by some modifications made to the recess geometry, which would result in a more uniform flow when the recesses are disposed into an array. The streamwise asymmetry, observed for the three velocity components and caused by the convection, could be avoided by elongating the recess in the upstream direction, making the geometry asymmetric, in such a way as to balance the convective effects: it must be observed, moreover, that the aforementioned asymmetry is stronger for the laminar case, meaning perhaps that the turbulent diffusion plays a role in balancing its value. Elongating the upstream wall would also mean an increase in the area where the lower skin friction was computed, which corresponds to the zone where the production of turbulent kinetic energy is greater. The increase in the values (both for spanwise and wall-normal velocities) on the trailing edge could be contrasted by decreasing the slope of the wall, a change that would also reduce the pressure drag as well as the variation of local pressure, resulting in a lower pressure gradient and less bending of the streamlines causing a variation in the spanwise motion and a more uniform spanwise flow in the streamwise direction. This variation would also affect the skin friction, since the modification of the downstream wall geometry would decrease the sharp change in speed observed in that area, going to affect not only the Reynolds shear stress but also the value of the turbulent kinetic energy production. The geometry modification suggested would improve the possible drag reduction performances of a recess, uniforming the flow and reducing the local peaks of skin friction and pressure drag. The turbulent and laminar cases are qualitatively similar, although some differences like the streamwise asymmetry and the range of values were found. The study of the laminar flow could lead to general information on the mean flow behavior, allowing to investigate different geometries with less computational costs. Nevertheless the turbulent properties appear to play a relevant role in the flow over the recess and thus have to be taken into account when designing a recess geometry for a dimples array.

References

- [1] V. V. Alekseev, I. A. Gachechiladze, G. I. Kiknadze, and V.G. Oleinikov. Tornado-like energy transfer on three-dimensional concavities of reliefs-structures of self organizing flow, their visualisation, and surface streamlining mechanism. In *Trans. 2nd Russian Net. Conf. Heat Trasfer, Heat Trasfer Intensification Radiation and Complex Heat Transfer*, volume 6, pages 33–42, 1998.
- [2] A. Bannier, E. Garnier, and P. Sagaut. Riblets Induced Drag Reduction on a Spatially Developing Turbulent Boundary Layer. In J. Jiménez, M. Stanislas, and I. Marusic, editors, *Prog. in Wall Turb. 2: Understanding and Modelling, Lille, France*, pages 213–224. Springer International Publishing, 2016.
- [3] N. Burgess and P. Ligrani. Effects Of Dimple Depth on Channel Nusselt Numbers and Friction Factors. *J. Heat Trans-T. ASME*, 127, 2005.
- [4] Y. Chen, Y. T Chew, and B. C. Khoo. Enhancement of heat transfer in turbulent channel flow over dimpled surface. *Int. J. Heat Mass Transf.*, 55(25):8100–8121, 2012.
- [5] J. Choi, W. P. Jeon, and H. Choi. Mechanism of drag reduction by dimples on a sphere. *Phys. Fluids*, 18(4):041702, 2006.

- [6] K. Fukagata, K. Iwamoto, and N. Kasagi. Contribution of Reynolds stress distribution to the skin friction in wall-bounded flows. *Phys. Fluids*, 14(11):L73–L76, 2002.
- [7] M. Gad-el-Hak. *Flow Control – Passive, Active and Reactive Flow Management*. Cambridge University Press, Cambridge, 2000.
- [8] F. Gattere, A. Chiarini, and M. Quadrio. Dimples for Skin-Friction Drag Reduction: Status and Perspectives. *Fluids*, 7(7):240, 2022.
- [9] J. Jeong and F. Hussain. On the identification of a vortex. *J. Fluid Mech.*, 285:69–94, 1995.
- [10] G.E. Karniadakis and K.-S. Choi. Mechanisms on transverse motions in turbulent wall flows. *Ann. Rev. Fluid Mech.*, 35:45–62, 2003.
- [11] G.V. Kovalenko, V.I. Terekhov, and A.A. Khalatov. Flow regimes in a single dimple on the channel surface. *J. Appl. Mech. Tech. Phys.*, 51(6):839–848, 2010.
- [12] H. Lienhart, M. Breuer, and C. Köksoy. Drag reduction by dimples? - A complementary experimental/numerical investigation. *Int. J. Heat Fluid Flow*, 29(3):783–791, 2008.
- [13] P. Luchini. Immersed-boundary simulation of turbulent flow past a sinusoidally undulated river bottom. *Eur. J. Mech. B / Fluids*, 55:340–347, 2016.
- [14] H. Mitsudharmadi, C. M. J. Tay, and H. M. Tsai. Effect of rounded edged dimple arrays on the boundary layer development. *J. Vis.*, 12(1):17–25, 2009.
- [15] J.H. Ng, R.K. Jaiman, T.T. Lim, C.M. Tay, and B.C. Khoo. Geometric Effects of Shallow Dimples in Turbulent Channel Flows at $Re_\tau \approx 180$: A Vorticity Transport Perspective. *Flow Turbul. Combust.*, 105:83–122, 2020.
- [16] Y. Peet and P. Sagaut. Theoretical prediction of turbulent skin friction on geometrically complex surfaces. *Phys. Fluids*, 2009.
- [17] M. Quadrio, B. Frohnapfel, and Y. Hasegawa. Does the choice of the forcing term affect flow statistics in DNS of turbulent channel flow? *Eur. J. Mech. B / Fluids*, 55:286–293, 2016.
- [18] M. Quadrio and P. Ricco. Critical assessment of turbulent drag reduction through spanwise wall oscillation. *J. Fluid Mech.*, 521:251–271, 2004.
- [19] M. Quadrio, P. Ricco, and C. Viotti. Streamwise-traveling waves of spanwise wall velocity for turbulent drag reduction. *J. Fluid Mech.*, 627:161–178, 2009.
- [20] M.A. Razzak, C. Yongdong, T.C.M. Jonathan, Z.W.A. Teo, T. Nadesan, K.B. Cheong, V.-T. Nguyen, D.J. Wise, K.T.E. Chua, and V.B.L. Boppana. Experimental study of skin-friction drag reduction of turbulent boundary layer over shallow dimples. In *AIAA Science and Technology Forum and Exposition, AIAA SciTech Forum 2022*, 2022.
- [21] N. Renard and S. Deck. A theoretical decomposition of mean skin friction generation into physical phenomena across the boundary layer. *J. Fluid Mech.*, 790:339–367, 2016.
- [22] F. Scarano, M. C. Jacob, R. Gojon, X. Carbonneau, and E. R. Gowree. Modification of a turbulent boundary layer by circular cavities. *Phys. Fluids*, 34(6):065134, 2022.
- [23] F. Scarano, M. C. Jacob, and E. R. Gowree. Drag reduction by means of an array of staggered circular cavities at moderate Reynolds numbers. *Int. J. Heat Fluid Flow*, 102:109142, 2023.
- [24] P.R. Spalart and J.D. McLean. Drag reduction: Enticing turbulence, and then an industry. *Phil. Trans. R. Soc. A*, 369(1940):1556–1569, 2011.
- [25] J. Szodrich. Viscous drag reduction on transport aircraft. In *29th Aerospace Sciences Meeting*, Aerospace Sciences Meetings. American Institute of Aeronautics and Astronautics, 1991.
- [26] C.M. Tay, Y.T. Chew, B.C. Khoo, and J.B. Zhao. Development of flow structures over dimples. *Exp. Therm. Fluid Sci.*, 52:278–287, 2014.
- [27] C.M.J. Tay, B.C. Khoo, and Y.T. Chew. Mechanics of drag reduction by shallow dimples in channel flow. *Phys. Fluids*, 27(3):035109, 2015.

- [28] C.M.J. Tay, T.T. Lim, B.C. Khoo, and R.K. Jaiman. Effectiveness of triangular depressions and asymmetric circular dimples for drag reduction. In *20th Australasian Fluid Mechanics Conference. Perth, Australia*, 2016.
- [29] O.W.G. Van Campenhout, M. Van Nesselrooij, Y. Y. Lin, J. Casacuberta, B. W. van Oudheusden, and S. Hickel. Experimental and numerical investigation into the drag performance of dimpled surfaces in a turbulent boundary layer. *Int. J. Heat Fluid Flow*, 100:109110, 2023.
- [30] O.W.G. Van Campenhout, M. Van Nesselrooij, L.L.M. Veldhuis, B.W. Van Oudheusden, and F.F.J. Schrijer. Flow visualization over drag reducing dimpled surfaces in turbulent boundary layers using Particle Image Velocimetry. In *18th International Symposium on the Application of Laser and Imaging Techniques to Fluid Mechanics*, pages 4–7, 2016.
- [31] O.W.G. Van Campenhout, M. Van Nesselrooij, L.L.M. Veldhuis, B.W. Van Oudheusden, and F.F.J. Schrijer. An experimental investigation into the flow mechanics of dimpled surfaces in turbulent boundary layers. In *2018 AIAA Aerospace Sciences Meeting*, page 2062, 2018.
- [32] M. Van Nesselrooij, O.W.G. Van Campenhout, B.W. Van Oudheusden, F.F.J. Schrijer, and L.L.M. Veldhuis. Development of an experimental apparatus for flat plate drag measurements and considerations for such measurements. *Meas. Sci. Technol.*, 33(5), 2022.
- [33] M. Van Nesselrooij, L.L.M. Veldhuis, B.W. Van Oudheusden, and F.F.J. Schrijer. Drag reduction by means of dimpled surfaces in turbulent boundary layers. *Exp. Fluids*, 57(9):142, 2016.
- [34] L. Veldhuis and E. Vervoort. Drag effect of a dented surface in a turbulent flow. In *27th AIAA Applied Aerodynamics Conference*, page 3950, 2009.

Abstract in lingua italiana

Il flusso turbolento su un recesso isolato è caratterizzato, come conseguenza del crescente interesse sulle cosiddette dimples, per ottenere informazioni sulla sua capacità di imporre al flusso un moto trasversale e ridurre l'attrito. Questo studio è basato su una simulazione DNS di un recesso circolare, posto all'interno di un canale, con un rapporto profondità/diametro di 0.05. Sono state eseguite simulazioni turbolente a $Re_\tau = 180$ e confrontate con il corrispondente caso laminare. Il flusso sulla cavità presenta un andamento convergente-divergente e genera un moto trasversale, causato principalmente dal gradiente di pressione, simile a quello osservabile con i cosiddetti metodi di riduzione d'attrito a forzamento trasversale. La presenza del recesso determina una variazione dell'attrito, con valori molto simili per le soluzioni laminari e turbolente nella metà a monte, ma con un comportamento diverso in quella a valle: la differenza nei risultati sembra essere legata a un aumento degli sforzi di Reynolds, che sono stati studiati utilizzando una variazione della decomposizione FIK [6] che ha permesso di separare l'attrito in una parte laminare e una turbolenta. Sono forniti infine alcuni suggerimenti su modifiche da apportare alla geometria del recesso in modo tale da poter, possibilmente, ottenere una riduzione di attrito.

Parole chiave: dimples, controllo del flusso, riduzione di attrito, turbolenza